Cellular and Molecular Bioengineering (2026) 19:225–248
https://doi.org/10.1007/s12195-026-00899-w

BMES BIOMEDICAL ENGINEERING SOCIETY

ORIGINAL ARTICLE

Graphene Nanoplatelets Suppress Foam Cell Formation and Atherogenic Inflammation in Macrophages

Farizah Hanim Lat[1] · Ahmad Naqib Shuid[1] · Mohd Yusmaidie Aziz[2] · Muhammad Azrul Zabidi[3] · Muhammad Mahyiddin Ramli[4] · Rafeezul Mohamed[1]

Received: 23 June 2025 / Accepted: 18 March 2026 / Published online: 3 April 2026

Abstract

Scope Foam cell formation is a hallmark of early atherosclerosis, driving plaque development and chronic vascular inflammation. These lipid-engorged macrophages form through excessive uptake of oxidised low-density lipoprotein (oxLDL) and play a central role in disease progression. Graphene nanoplatelets (GNPs), known for their high surface area and biocompatibility, have emerged as promising nanomaterials for biomedical intervention. This study evaluates the potential of GNPs to prevent atherosclerosis by targeting foam cell formation.

Methods Computational analyses, including molecular docking and dynamics simulations, were used to assess the binding affinity of GNPs with key atherogenic proteins such as apolipoprotein B and the LDL receptor. GNPs were structurally characterised using Raman spectroscopy, X-ray diffraction, and Fourier-transform infrared spectroscopy. In vitro assays were conducted on RAW264.7 macrophages to assess cytotoxicity, lipid accumulation, cholesterol levels, cytokine production, and gene expression after treatment with GNPs (1 μg/mL) and oxLDL.

Results GNPs exhibited strong binding affinity to apoB and the LDL receptor, suggesting potential interference with lipid uptake. Structural analyses confirmed the integrity and purity of the GNPs. In vitro, GNPs showed no cytotoxic effects and significantly reduced lipid accumulation and intracellular cholesterol levels in oxLDL-treated macrophages. They also suppressed the secretion of pro-inflammatory cytokines (IFNγ, IL-6, IL-1β) and downregulated genes associated with foam cell formation (IL-1β, ACAT-1, CD36), while upregulating ABCA1, a key gene involved in cholesterol efflux.

Conclusion These findings demonstrate that GNPs effectively inhibit foam cell formation, reduce atherogenic inflammation, and enhance lipid clearance in macrophages. GNPs represent a promising nanotherapeutic strategy for the prevention of atherosclerosis.

Keywords Atherosclerosis · Graphene nanoplatelets · Macrophages · Oxidised low density lipoprotein · Foam cells

Associate Editor Tamara L. Kinzer-Ursem oversaw the review of this article.

✉ Rafeezul Mohamed
rafeezul@usm.my

1 Department of Biomedical Science, Pusat Kanser Tun Abdullah Ahmad Badawi, Universiti Sains Malaysia, Bertam, 13200 Kepala Batas, Pulau Pinang, Malaysia

2 Department of Toxicology, Pusat Kanser Tun Abdullah Ahmad Badawi, Universiti Sains Malaysia, Bertam, 13200 Kepala Batas, Pulau Pinang, Malaysia

3 Department of Dental Science, Pusat Kanser Tun Abdullah Ahmad Badawi, Universiti Sains Malaysia, Bertam, 13200 Kepala Batas, Pulau Pinang, Malaysia

4 Institute of Nano Electronic Engineering, Universiti Malaysia Perlis, 01000 Kangar, Perlis, Malaysia

Introduction

Atherosclerosis, a chronic arterial disease, is a leading cause of ischemic stroke, myocardial infarction, and unstable angina, often progressing silently over many years before manifesting as acute cardiovascular events [1]. Despite advancements in treatments such as surgical interventions and the management of hyperlipidemia and hypertension, it remains a major global cause of mortality, underscoring the urgent need for novel therapeutic strategies [2]. The disease progresses through three stages: lipid streaks, fibrous plaques, and advanced lesions with thrombosis [2]. Early lipid accumulation in arterial walls triggers macrophage infiltration and foam cell formation, initiating atherogenesis [3]. As vascular smooth muscle cells migrate and form

fibrous caps over atherosclerotic sites, plaques stabilize, although necrosis within the plaques may occur [4]. In advanced stages, expansion of necrotic cores and interactions with coagulation factors significantly increase the risk of thrombosis [5]. Foam cell formation, a pivotal process in atherogenesis, results from an imbalance in lipid homeostasis. Excessive lipid uptake via scavenger receptors (SRs) such as CD36, SRA-1, LOX-1, and Toll-like receptor 4 (TLR4) and impaired lipid efflux mediated by transporters like ABCA1 and ABCG1 contribute to macrophage dysfunction, inflammation, and plaque progression [6, 7]. However, the intricate mechanisms underlying these pathways remain inadequately understood, limiting the development of effective targeted therapies [8].

Nanoparticle-based strategies have shown promise in modulating macrophage behavior in atherosclerosis. Zhang et al. demonstrated that biodegradable PLGA-b-PEG nanoparticles carrying a Liver X receptor (LXR) agonist preferentially accumulated in plaque macrophages, enhancing cholesterol efflux gene expression and suppressing inflammatory signaling [9]. LXRs are nuclear receptors that regulate cholesterol metabolism and inflammation in macrophages, and their activation has been shown to attenuate atherosclerosis; however, systemic administration of free LXR agonists can cause adverse effects, such as hepatic steatosis and elevated triglycerides [9]. These nanoparticles delivered GW3965 directly to plaque macrophages, improved LXR target gene expression and anti-inflammatory responses in vitro, and reduced macrophage content in plaques by ~ 50% in LDLR$^{-/-}$ mice without causing liver toxicity [9].

Complementing these drug-loaded strategies, Tang et al. developed a high-throughput library of HDL-mimicking nanoparticles with varied compositions to systematically evaluate how physicochemical properties influence targeting of specific immune cell types [10]. Using ApoE$^{-/-}$ mice, they assessed nanoparticle accumulation in macrophages via flow cytometry, near-infrared imaging, and PET/CT, identifying formulations that preferentially targeted plaque macrophages while minimizing off-target uptake [10]. These studies highlight that both nanoparticle design and material properties critically affect foam cell modulation and inflammatory signaling [10]. Building on these insights, our study investigates whether graphene nanoplatelets, through their intrinsic physicochemical characteristics, can suppress macrophage foam cell formation and atherogenic inflammation without the need for drug loading or surface functionalization. To achieve this, we combined computational modeling with experimental validation to elucidate how graphene nanoplatelets modulate macrophage lipid handling and inflammatory pathways.

Graphene nanoplatelets (GNPs) offer a unique combination of physicochemical properties, including high surface area, mechanical stability, and intrinsic ability to interact with biomolecules such as apolipoprotein B (ApoB) and low-density lipoprotein receptor (LDLR), making them promising candidates for modulating macrophage foam cell formation. Unlike polymeric or other non-metallic nanoparticles, GNPs do not require encapsulated drugs or synthetic ligands to exert potential biological effects, which may reduce formulation complexity and off-target interactions [11, 12]. These features provide a mechanistic rationale for investigating GNPs as a novel nanomaterial in the context of atherosclerosis.

Importantly, prior in vivo studies provide supporting evidence for the biomedical applicability and biocompatibility of graphene-based materials. Graphene derivatives have been extensively investigated in animal models of neural regeneration and spinal cord injury, where they demonstrated favorable tissue integration, modulation of inflammatory responses, and acceptable in vivo biocompatibility [13]. In parallel, in vivo toxicological evaluations of graphene oxide nanoplatelets have shown that these materials can be systemically tolerated at controlled doses, without inducing significant adverse effects in major organs or hematological parameters, supporting their translational feasibility [14]. Furthermore, comprehensive analyses of graphene nanomaterials have emphasized that in vivo safety and biological responses are strongly influenced by physicochemical characteristics such as particle size, surface chemistry, and dose, with appropriately engineered graphene-based materials exhibiting acceptable biocompatibility profiles [15]. Although these studies primarily focused on neurological or toxicological applications rather than cardiovascular disease, the demonstrated in vivo biocompatibility and inflammation-modulating properties of graphene-based materials provide a strong rationale for investigating GNPs in other inflammation-driven pathologies, including atherosclerosis and macrophage foam cell formation.

Low-density lipoprotein (LDL) itself is a naturally occurring nanoscale particle whose biological behavior is governed by ApoB-100, the primary structural protein responsible for LDL recognition and internalization via the LDLR and other lipid-handling receptors on target cells, including macrophages [12, 16]. Recent studies with LDL-based nanoparticles have shown that these particles preferentially accumulate in atherosclerotic plaques and are taken up by intimal macrophages, exploiting native ApoB-mediated interactions involving LDLR and scavenger receptors such as CD36 and SR-A [11]. These findings suggest that nanoparticle interactions with ApoB or LDLR may elicit biological responses analogous to those triggered by native LDL particles, including cholesterol trafficking, foam cell modulation, and regulation of inflammatory signaling [12]. Notably, these LDL-mimicking nanoparticles achieved targeting without the need for synthetic ligands, highlighting the sufficiency of ApoB itself as a biological targeting ligand [11, 12]. Based on this emerging paradigm, we hypothesize that GNPs, owing to their large surface area and intrinsic physicochemical characteristics, may interact with ApoB or ApoB-associated LDL

complexes and thereby influence LDLR-mediated lipid uptake, scavenger receptor pathways (CD36/SR-A), and macrophage foam cell formation. This hypothesis provides a mechanistic rationale for investigating GNP interactions with ApoB and LDLR in the context of atherosclerosis, bridging insights from native LDL behavior, LDL-mimicking nanoparticles, and potential GNP effects on foam cell biology.

Our prior computational studies demonstrated that pristine graphene exhibits strong binding affinities with atherosclerosis-related receptors, particularly TLR4 (− 13.3 kcal/mol), followed by LOX-1 (− 11.3 kcal/mol), SRA-1 (− 11.2 kcal/mol), and CD36 (− 10.7 kcal/mol) [17]. These findings suggested that graphene could modulate receptor activity, influencing pathways critical to foam cell formation and inflammation. Building on these computational insights, the current study was designed to investigate commercially available GNPs, which share structural features with pristine graphene, for their potential to interact with ApoB, LDLR, and SRs. This rationale directly connects our prior in silico findings with the experimental and modeling work presented here, providing a clear mechanistic basis for exploring GNPs as modulators of macrophage foam cell formation and inflammatory signaling.

Graphene, a single layer of sp2-hybridized carbon atoms arranged in a hexagonal lattice, was first isolated in 2004 and has since emerged as a promising material for various biomedical applications due to its unique physicochemical properties and biocompatibility [18, 19]. Applications of graphene-based materials include biosensing, drug delivery, photothermal therapy, and tissue engineering. Among these materials, GNPs stand out for their cost-effectiveness and practicality in experimental applications. GNPs, consisting of monolayer and multilayer graphene (2–10 layers) along with nanostructured graphite, are commercially available and offer a broad thickness range of 0.34–100 nm [20, 21]. Their large specific surface area enhances interaction and load transfer in biological systems, making them an attractive choice over other nanomaterials like carbon nanotubes [21]. Graphene-based nanomaterials have attracted significant interest in biomedical research due to their unique physicochemical properties and potential for diverse applications. Specifically, GNPs have gained attention for their accessibility and cost-effectiveness, further reinforcing their value in experimental studies.

Macrophages interact with nanoparticles via cell-surface receptors, including SRs, which are crucial for processes like phagocytosis and immune regulation [22]. Among these receptors, CD36 is particularly significant in mediating the uptake of oxidized low-density lipoprotein (oxLDL), a key event in foam cell formation and the associated inflammatory responses [23]. When CD36 binds to its ligands, it triggers intracellular signaling cascades that regulate energy metabolism, mitochondrial activity, apoptosis, and oxidative stress, ultimately shaping macrophage behavior [23]. These interactions suggest that nanoparticles, such as graphene nanoplatelets, may inhibit oxLDL uptake, offering potential strategies to prevent atherosclerotic plaque development.

Building on these computational insights, this study integrates predictions with experimental validation to explore the potential of commercially available GNPs in modulating atherogenesis. The GNPs used were selected to align structurally with the graphene models used in silico. They were characterized using Raman spectroscopy, XRD, and FTIR to confirm their structural properties. Subsequently, in vitro assays, including cell viability, Oil Red O staining, total cholesterol estimation, ELISA, and gene expression analysis, were employed to assess their biocompatibility and effects on foam cell formation. By bridging computational insights with experimental evidence, this study provides a comprehensive understanding of graphene's interaction with atherosclerosis-related receptors, including LDLR and ApoB. These findings highlight the potential of graphene-based nanomaterials, particularly commercially available GNPs, in modulating foam cell formation and offer promising prospects for their application in atherosclerosis management.

Materials and Methods

Selection and Preparation of Target Proteins

Three-dimensional structures of the low-density lipoprotein receptor (LDLR; PDB ID: 1AJJ) were retrieved from the Protein Data Bank, while the apolipoprotein B (ApoB; UniProt ID: P04114) sequence was obtained from the UniProt database. Prior to docking analysis, protein structures were prepared using AutoDockTools by removing crystallographic water molecules and non-essential structural components. Hydrogen atoms and partial charges were added as required, and the finalized protein structures were converted into PDBQT format for subsequent docking studies. To identify potential ligand-binding regions, all protein structures were analyzed using the P2Rank algorithm, which predicts ligandable pockets based on surface geometry and physicochemical features. The highest-ranked binding pockets predicted by P2Rank were selected and used as target sites in the docking simulations [24].

Construction of Graphene Models

GNP models were constructed based on previously reported structural parameters and publicly available references, including industrial and academic sources. Two-dimensional graphene representations were generated and cross-validated using the PubChem database to ensure structural consistency. The finalized graphene structures were saved in Structure Data File (SDF) format to enable compatibility with downstream computational analyses [25].

Active Site Identification

Ligand-binding regions within the protein structures were analyzed using PrankWeb, the web-based implementation of the P2Rank algorithm, to improve confidence in binding site selection. Identified pockets, including the most ligandable regions in both LDLR and ApoB, were used to define the spatial location and dimensions of grid boxes for molecular docking. The combined use of P2Rank and PrankWeb allowed for a robust identification of plausible ligand interaction sites by integrating surface topology, electrostatic properties, and machine-learning–based ligandability scoring [24, 26].

Molecular Docking Analysis

Molecular docking simulations were carried out using AutoDock Vina to evaluate interactions between graphene nanoplatelets and the selected protein targets [27]. Grid box parameters were defined based on the predicted active sites, and docking simulations were performed to explore energetically favorable binding configurations. Binding affinities were reported as docking scores (kcal/mol), with more negative values indicating stronger predicted interactions between graphene models and target proteins.

Interaction and Binding Analysis

The resulting protein-graphene complexes were visualized and analyzed using PyMOL to examine binding orientation and surface interactions. In addition, BINANA version 2.2 was employed to identify and characterize intermolecular interactions, including hydrogen bonding, hydrophobic contacts, and π-related interactions [28]. PDBQT files containing polar hydrogens and partial charges served as input for BINANA analysis, which also enabled detection of intramolecular interactions within the protein–ligand complexes.

Molecular Dynamics Simulations

Molecular dynamics (MD) simulations were conducted to assess the stability and dynamic behavior of protein-graphene complexes using GROMACS 2023 on a Linux-based computational platform. The CHARMM36 force field was applied to generate system topologies, and protein parameters were prepared using the pdb2gmx module. Each system was solvated in an explicit water box, and electrical neutrality was achieved by adding sodium and chloride ions using the genion tool.

Energy minimization was performed for up to 50,000 steps to eliminate unfavorable contacts and stabilize the system. Following minimization, equilibration was carried out in two phases: first under constant volume and temperature (NVT) conditions at 300 K for 1000 ps, and subsequently under constant pressure and temperature (NPT) conditions for an additional 1000 ps to stabilize pressure and density.

A production MD simulation was then performed for 100 ns, during which structural stability and conformational changes were monitored. Key parameters, including root mean square deviation (RMSD), root mean square fluctuation (RMSF), and radius of gyration (Rg), were calculated and analyzed using qtgrace to evaluate the dynamic behavior of the protein–graphene complexes.

Binding Free Energy Estimation

Binding free energies of the protein–graphene complexes were estimated using the Molecular Mechanics Poisson–Boltzmann Surface Area (MM-PBSA) approach. The calculations were carried out by post-processing equilibrated molecular dynamics trajectories to quantify the energetic contributions associated with complex formation.

The binding free energy (ΔG_bind) was determined according to the following relationship:

$$\Delta G_{bind} = \Delta G_{complex} - \left(\Delta G_{protein} + \Delta G_{ligand}\right)$$

where $\Delta G_{complex}$ represents the total free energy of the protein–ligand complex, $\Delta G_{protein}$ corresponds to the free energy of the isolated protein, and ΔG_{ligand} denotes the free energy of the ligand alone.

The total binding free energy was decomposed into individual energy components, including molecular mechanics terms and solvation energies. Molecular mechanics contributions consisted of van der Waals and electrostatic interactions, while solvation effects were evaluated using the Poisson–Boltzmann model for polar solvation and solvent-accessible surface area (SASA) calculations for nonpolar solvation contributions. This energy decomposition enabled identification of the dominant interactions governing complex stability and binding affinity between the graphene nanoplatelets and target protein receptors.

Cell Line, Culture Conditions, and Reagents

The murine macrophage cell line RAW264.7 was obtained from the American Type Culture Collection (ATCC, Manassas, VA, USA). Cells were maintained in RPMI-1640 medium supplemented with 10% fetal bovine serum (FBS) and 1% penicillin–streptomycin, and incubated at 37 °C in a humidified atmosphere containing 5% CO_2. OxLDL and GNPs (2-10 nm) were procured from Thermo Fisher Scientific (Waltham, MA, USA).

Characterization of Graphene Nanoplatelets

The structural and chemical properties of GNPs were evaluated using multiple complementary techniques. Raman spectroscopy (Witec Alpha 300R, WITec GmbH, Germany) was used to assess layer structure and quality. X-ray diffraction (XRD), (D2 Phaser, Bruker, Billerica, MA, USA) was employed to determine the crystalline phase, while Fourier-transform infrared spectroscopy (FTIR), (PerkinElmer, Waltham, MA, USA) was used to identify surface functional groups.

Cell Viability Assay

Cellular viability in response to GNPs exposure was determined using the PrestoBlue™ reagent (Thermo Fisher Scientific, Waltham, MA, USA). RAW264.7 cells were seeded at a density of 5×10^4 cells/well in 96-well plates and allowed to adhere overnight. Cells were then treated with GNPs at concentrations ranging from 0.1 to 50 μg/mL for 24, 48, and 72 h. After treatment, the medium was removed, cells were washed with phosphate-buffered saline (PBS), and a mixture of 10 μL PrestoBlue™ reagent with 90 μL fresh RPMI medium was added per well. Plates were incubated in the dark at 37 °C for 50 min, and fluorescence was measured at excitation/emission wavelengths of 540–570 and 544–590 nm, respectively, using a FLUOstar Omega microplate reader (BMG Labtech, Ortenberg, Germany). Blank readings were subtracted, and cell viability was expressed as a percentage of untreated controls.

RAW264.7 Cells Treated with oxLDL, GNPs and Combination of oxLDL and GNPs

RAW264.7 macrophages were cultured in complete RPMI medium containing 10% FBS and 1% penicillin-streptomycin and were first incubated for 24 h to allow cell attachment. Following this, cells were treated with either 100 μg/mL of oxLDL, 1 μg/mL of GNPs, or a combination of both administered concurrently for 24 and 48 h. This treatment design allows assessment of GNPs' ability to prevent foam cell formation during lipid uptake rather than reversing pre-formed foam cells. The treated cells were collected at respective times for further use in following experiments.

Oil Red O Staining

To visualize intracellular lipid deposits, cells were fixed in 10% formaldehyde for 30 min and washed twice with PBS. Cells were pre-treated with 60% 2-propanol for 15 s to enhance staining, then incubated with 0.2% Oil Red O solution in 60% 2-propanol for 50 min. Excess dye was removed with brief 2-propanol washes, followed by two PBS washes. Nuclear counterstaining was performed with Mayer's hematoxylin for 1 min. Lipid droplets and nuclei were visualized under an Olympus LX51 inverted microscope at 40× magnification. Quantitative analysis of lipid accumulation was performed using ImageJ software (NIH, USA). Images were converted to 8-bit grayscale, and background noise was reduced using the *Subtract Background* function. Lipid droplets were segmented using a consistent threshold across all samples and converted into binary images. The *Analyze Particles* function was applied to quantify Oil Red O-positive area, droplet number, and droplet size. Lipid accumulation was expressed as the percentage of Oil Red O-positive area relative to the total cell area.

Cholesterol and Cholesteryl Ester Quantification

Total cholesterol (free cholesterol plus cholesteryl esters) in treated cells was measured using a Cholesterol/Cholesteryl Ester Quantitation Kit (Abcam, Cambridge, MA, USA) according to the manufacturer's instructions. Briefly, 50 μL of cell lysate diluted in reaction buffer was mixed with 50 μL of either the total or free cholesterol assay mixture in a 96-well plate and incubated at 37 °C for 60 min in the dark. Fluorescence was measured at 535 nm excitation and 595 nm emission using a FLUOstar Omega plate reader (BMG Labtech, Ortenberg, Germany).

Enzyme-Linked Immunosorbent Assay (ELISA)

The concentrations of pro-inflammatory cytokines IFNγ, IL-6, IL-1β, and TNF-α in the culture supernatants of treated RAW264.7 cells were measured using the Mouse ELISA Kit Ready Set Go (Bio-Techne, Minneapolis, MN, USA) following the manufacturer's instructions. For each cytokine, 96-well plates were coated with the corresponding capture antibody and incubated at 4 °C overnight. After coating, plates were washed three times with 300 μL wash buffer per well, and a blocking step was performed by adding diluent buffer and incubating at room temperature for 1 h. The diluent buffer was then removed, followed by two washes with wash buffer. Serial dilutions of standards were prepared in eight concentrations for each cytokine, and samples along with blanks were added to the appropriate wells. Plates were sealed and incubated at 4 °C overnight. After incubation, plates were washed four times to remove unbound proteins. Detection antibodies specific for each cytokine were added and incubated at room temperature for 1 hour, followed by four washes. Avidin-HRP was then added to each well and incubated at room temperature for 30 min. Plates were washed six times to remove unbound enzyme conjugate. Subsequently, 1× TMB substrate solution was added and incubated at room temperature for 15 min to allow color

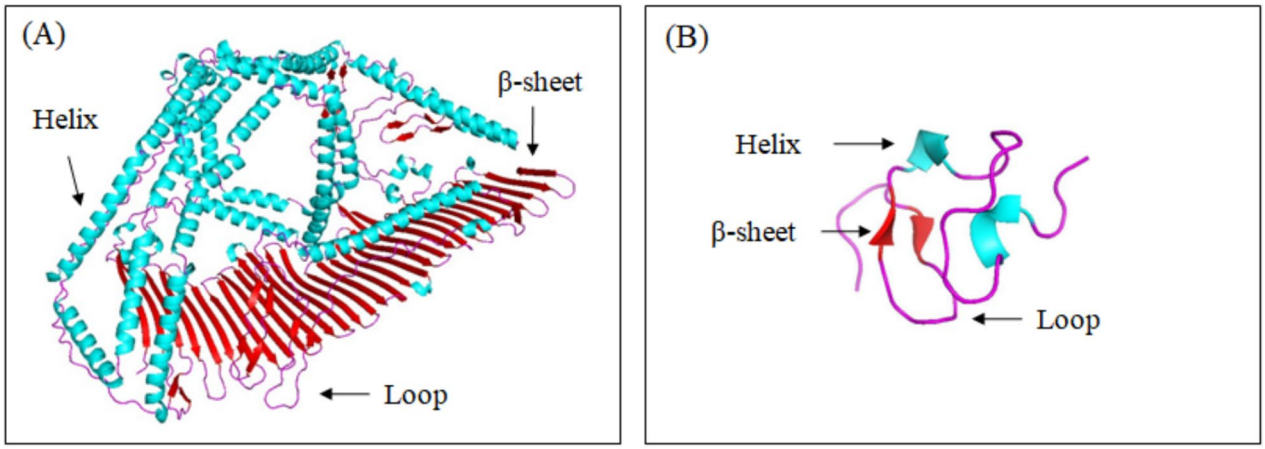

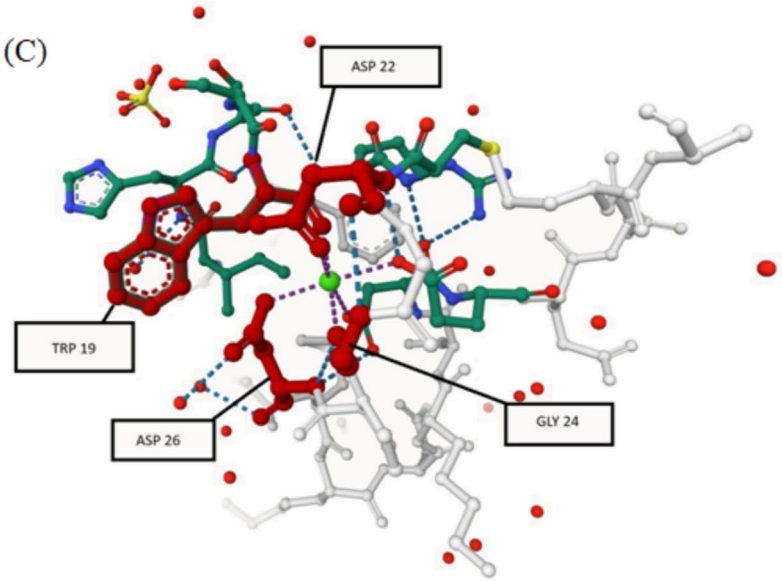

(D)

Metric	APOB (Large Segment)	1AJJ (LR5 Domain)
Total Residues	1,400 [3]	37 [4444]
Alpha Helix %	37.6% [5]	0.0% [666]
Beta Sheet %	36.2% [7]	10.8% [8]
Loop/Turn %	26.2% [9999]	72.9% [10101010]
Helix:Sheet Ratio	1.04 : 1	0:01

◂**Fig. 1** Structural representation of ApoB-100 and LDL receptor. **A** Simplified three-dimensional structure of an ApoB-100 large segment, highlighting secondary structural elements: helical regions (cyan), β-sheet regions (red), and loops/turns (magenta). **B** Simplified three-dimensional structure of the LDL receptor ligand-binding domain (LR5), shown using a distinct color scheme for clarity. **C** Close-up view of the LDL receptor binding region illustrating key interacting residues (TRP19, ASP22, GLY24, ASP26) involved in ligand interactions. **D** Quantitative comparison of secondary structure composition between the ApoB-100 large segment and the LDL receptor LR5 domain

development. The reaction was stopped using the provided stop solution, and absorbance was measured at 450 nm with 570 nm as the reference wavelength using a FLUOstar Omega microplate reader (BMG Labtech, Ortenberg, Germany). Cytokine concentrations were calculated by comparing sample absorbance to standard curves.

Total RNA Extraction and cDNA Synthesis

Total RNA was isolated from treated RAW264.7 cells using TRIzol™ reagent (Invitrogen Life Technologies, Carlsbad, CA, USA) according to the manufacturer's protocol. RNA purity and concentration were evaluated using a NanoDrop spectrophotometer, with A260/A280 ratios between 1.7 and 1.9 considered acceptable for downstream applications. RNA integrity was confirmed by agarose gel electrophoresis, which showed clear 28S and 18S rRNA bands.

For cDNA synthesis, 2 µg of RNA was reverse-transcribed using the Tetro cDNA Synthesis Kit (Bioline, London, UK) in a total reaction volume of 20 µL. The reaction mixture included RNA, oligo(dT)18 primers, 10 mM dNTPs, 5 × RT buffer, RNase inhibitor, Tetro Reverse Transcriptase, and DEPC-treated water. The reaction was gently mixed, incubated at 45 °C for 30 minutes, then terminated by heating at 85 °C for 5 min and cooled on ice. Successful cDNA synthesis was verified by PCR amplification of the GAPDH gene (110 bp) prior to further analysis.

Quantitative Real-Time Polymerase Chain Reaction (qRT-PCR)

Gene expression analysis was performed using the SensiFAST SYBR Hi-Rox Kit (Bioline, London, UK) on a StepOnePlus Real-Time PCR System (Applied Biosystems, Foster City, CA, USA). Each 20 µL reaction contained 10 µL of 2 × SYBR mix, 0.8 µL of 10 µM forward and reverse primer mix, 2 µL cDNA template, and 6.4 µL nuclease-free water.

Thermal cycling conditions consisted of an initial denaturation at 95 °C for 2 min, followed by 40 cycles of 95 °C for 5 s and 60 °C for 30 s. The primer sequences used for target genes were:

IL-1β: Forward 5′-AAGGAGAACCAAGCAACGACAAAA-3′, Reverse 5′-TGGGGAACTCTGCAGACTCAAACT-3′

ABCA1: Forward 5′-TGAAGCCTGTCCAGGAGTTC-3′, Reverse 5′-ATGACAAGGAGGATGGAAGC-3′

ACAT1: Forward 5′-GCAGGGAAGTTTGCCAGTGAGA-3′, Reverse 5′-GAACACGGTCTTGAGCTTTGGC-3′

CD36: Forward 5′-TTTCCTCTGACATTTGCAGGTTCTA-3′, Reverse 5′-AAAGGCATTGGCTGGAAGGAA-3′

Relative mRNA expression levels were calculated using the ΔΔCt method, with GAPDH serving as the internal reference gene.

Statistical Analysis

All experiments were performed in triplicate, and data are presented as mean ± standard deviation (SD). Statistical analyses were conducted using GraphPad Prism Version 6.01. Comparisons between multiple groups were carried out using one-way analysis of variance (ANOVA) followed by Tukey's post hoc test. Differences were considered statistically significant at $P < 0.05$. Significance levels are indicated as follows: n.s., not significant; *$P \leq 0.05$; **$P \leq 0.01$; ***$P \leq 0.001$; ****$P \leq 0.0001$.

Results

Structural Role of ApoB-100 and LDLR in Atherosclerosis: A Foundation for Nanomaterial Interaction Studies

The ApoB-100 (Fig. 1A) and LDLR (Fig. 1B) are essential components in cholesterol metabolism and are intricately linked to the development of atherosclerosis [29, 30]. ApoB-100, encoded by the APOB gene (UniProt ID: P04114), is a large glycoprotein consisting of 4563 amino acids. It is the principal structural and functional protein of low-density lipoproteins (LDL), playing a critical role in facilitating LDL recognition and internalization by hepatocytes through receptor-mediated endocytosis [29].

As shown in Fig. 1A, the simplified three-dimensional structure of ApoB-100 reveals a heterogeneous secondary structure composition, dominated by helical regions (cyan), interspersed with β-sheet regions (red) and loop/turn regions (magenta). Quantitative analysis of secondary structural elements (Fig. 1D) indicates that helical regions constitute the largest proportion of the ApoB-100 structure, followed by β-sheet and loop components, reflecting

the flexible and extended conformation required for LDL particle assembly and receptor interaction.

However, oxidative modifications of LDL result in the formation of oxLDL, which alters the structure of ApoB-100. These changes impair its binding affinity for LDLR and shift its interactions toward scavenger receptors such as LOX1 and CD36, ultimately leading to foam cell formation and the progression of atherosclerosis. Moreover, genetic polymorphisms in APOB, such as those defining the low-density lipoprotein cholesterol level quantitative trait locus 4 (LDLCQ4), are associated with variations in cholesterol metabolism, further increasing susceptibility to cardiovascular diseases [29].

The LDL receptor, particularly its ligand-binding module 5 (LB5; PDB ID: 1AJJ), is a transmembrane glycoprotein critical for LDL uptake [30]. Figure 1B presents the simplified three-dimensional structure of the LDLR LB5 domain, with the ligand-binding region explicitly highlighted. LB5 directly interacts with ApoB-100 on the surface of LDL particles, mediating their clearance from circulation. A detailed view of the binding interface (Fig. 1C) identifies key residues involved in ligand recognition, including TRP19, ASP22, GLY24, and ASP26, which collectively define the functional binding region of the receptor. Structural studies of LB5 have highlighted its specificity for ApoB-100, underscoring its essential role in regulating cholesterol levels [30]. Dysfunction in LDLR, whether due to genetic mutations or oxidative damage, leads to impaired LDL clearance and contributes to the formation of atherogenic plaques [30].

In this study, ApoB-100 was selected as a representative for both native LDL and oxLDL due to its central role in LDL receptor recognition and its susceptibility to oxidative modifications, which are key processes in atherogenesis. Similarly, the LDLR's LB5 module was chosen as a model for understanding receptor functionality in LDL clearance. These biomolecules were analyzed through molecular docking and molecular dynamics (MD) simulations to elucidate how nanomaterials, such as graphene, interact with LDL and LDLR. By investigating these interactions, the study aimed to assess graphene's potential in modulating cholesterol transport, foam cell formation, and atherogenesis. Together, ApoB-100 and LDLR provide critical insights into the mechanisms underlying atherosclerosis and are invaluable for studying the impact of nanomaterials in mitigating disease progression. Their structural and functional roles make them ideal targets for computational and experimental studies aimed at developing novel therapeutic interventions.

Molecular Docking and Interaction Analysis of Atherosclerosis-Related Proteins with Graphene

A molecular docking study, as summarized in Table 1, assessed the binding affinities of graphene with two critical proteins involved in atherosclerosis: ApoB and the LDLR. The results showed that graphene exhibited a strong binding affinity with ApoB (− 12.9 kcal/mol), suggesting significant interactions with the structural and functional domains of this key component of LDL particles. The interaction analysis, depicted in Fig. 2B, revealed critical T-stacking interactions with residues TYR111, PHE107, and PHE390 (indicated by aqua dashed lines). These interactions play a crucial role in stabilizing graphene's binding to ApoB and underscore its potential to disrupt LDL metabolism by interacting with its structural components.

In contrast, graphene's binding affinity with LDLR was moderate (− 8.4 kcal/mol). Although weaker than its interaction with ApoB, the binding remains biologically relevant due to LDLR's role in LDL clearance. The interaction analysis, illustrated in Fig. 2A, revealed key T-stacking interactions with residues TRP22 and HIS19 (aqua dashed lines) and cation-π interactions with HIS19 (navy dashed lines). Hydrophobic interactions, represented by gray spheres, further contributed to the binding stability between graphene and LDLR. These findings suggest that graphene preferentially binds to ApoB over LDLR, highlighting its potential to interfere with LDL structural components while still interacting with its receptor.

Building on these findings, prior computational studies by Lat et al. [17] demonstrated that pristine graphene exhibits strong binding affinities with other atherosclerosis-related receptors, particularly TLR4 (− 13.3 kcal/mol), LOX-1 (− 11.3 kcal/mol), SRA1 (− 11.2 kcal/mol), and CD36 (− 10.7 kcal/mol) [17]. Graphene's interaction with TLR4 and CD36 was dominated by hydrophobic forces, emphasizing its ability to modulate inflammatory and lipid uptake

Table 1 Binding energy analysis of LDL receptor and ApoB protein with the graphene model (GM)

Proteins	Ligand	Average binding energy (kcal/mol)	Standard deviation (kcal/mol)	Standard error of mean (kcal/mol)
LDL receptor	Graphene model (GM)	− 8.4	0.05164	0.04083
ApoB protein		− 12.9	0.040825	0.040825

This table presents the average binding energy, standard deviation, and standard error of the mean for the interactions of LDL receptor and ApoB protein with graphene model. These findings suggest a stronger affinity of graphene towards the ApoB protein, possibly due to its larger size and greater interaction surface

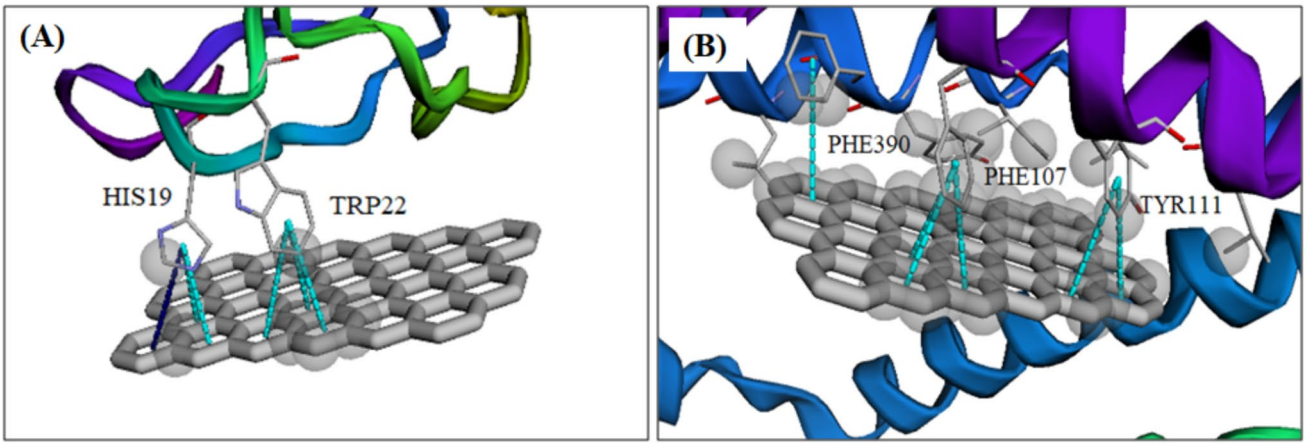

Fig. 2 Detailed interaction analysis using BINANA which identifies and visualizes ligand-receptor interactions in the binding regions. **A** LDLR and **B** ApoB protein with graphene model. The interactions are marked by different symbols and colours: aqua dashed lines represent π-stacking interactions, navy blue dashed lines represent cation-π interactions, and gray spheres denote hydrophobic interactions. This representation is schematic and intended to visualize interaction types; interatomic distances are not drawn to scale. Docking was performed in multiple replicates, and the top-ranked pose from a representative run was selected for detailed interaction analysis

pathways. Additionally, the cation-π interaction between the LYS199 residue of SRA1 and graphene provided critical stabilization to the complex. Similarly, interactions with LOX-1 included cation-π interactions with ARG208 and π-stacking interactions with TRP215, further underscoring graphene's potential to interfere with LDL uptake and signaling pathways.

Taken together, these results demonstrate that graphene interacts with atherosclerosis-related proteins through diverse mechanisms, including T-stacking, cation-π, and hydrophobic interactions. The strongest affinities were observed for ApoB and TLR4, indicating graphene's potential to disrupt both LDL particle stability and inflammatory pathways. By combining insights from current and prior studies, these findings highlight the multifaceted nature of graphene's interactions and its potential impact on atherosclerosis progression.

Molecular Dynamics Simulation of Atherosclerosis-Related Protein with Graphene Interactions

The root mean square deviation (RMSD) analysis provided insights into the stability and conformational changes of the protein-graphene complexes (Fig. 3A). For the LDL receptor, the average RMSD was approximately 0.2426 nm, with a peak value of 0.4196 nm at 66.47 ns, indicating stable interactions with minimal structural fluctuations. The ApoB protein, however, exhibited higher flexibility with an average RMSD of 1.7124 nm and a peak value of 2.1365 nm at 96.55 ns, reflecting greater structural adaptation during its interaction with graphene. Comparatively, the RMSD values for CD36 (0.199 nm), LOX1 (0.264 nm), TLR4 (0.351 nm), and SRA1 (1.304 nm) from previous simulations [17] indicated varying degrees of stability, with CD36 showing the least structural fluctuations and SRA1 the highest among these proteins.

The radius of gyration (Rg) analysis revealed differences in compactness and conformational stability (Fig. 3B). The LDL receptor maintained a compact structure with an average Rg of 0.9247 nm, while ApoB displayed a more extended conformation with an Rg of 4.5953 nm. Previous studies by Lat et al. reported Rg values of 1.688 nm for SRA1, 2.073 nm for LOX1, 2.243 nm for CD36, and 3.114 nm for TLR4 [17]. These findings suggest that ApoB's larger size and extended structure result in higher Rg values compared to other proteins.

The root mean square fluctuation (RMSF) analysis highlighted the flexibility of specific residues within the protein-graphene complexes (Fig. 3C, D). For the LDL receptor, notable fluctuations were observed around residues 7–8 and 19–27, with significant interactions occurring at residues HIS19 and TRP22. ApoB protein exhibited prominent flexibility at residues 93–129 and 366–398, with key binding interactions at residues PHE107, TYR111, and PHE390, which contributed to its stability and higher binding affinity with graphene.

These findings align with prior computational studies by Lat et al. [17], where CD36 demonstrated the most stable interactions with graphene due to low RMSD (0.199 nm) and moderate Rg (2.243 nm), while TLR4 had the highest Rg (3.114 nm) among all proteins [17]. The results collectively underscore the varying interaction dynamics of different proteins with graphene, with ApoB and TLR4 showing

higher flexibility and structural adaptation, while LDLR and CD36 demonstrated more compact and stable interactions.

Binding Free Energy Analysis of Graphene with Atherosclerosis-Related Protein Using MM-PBSA

The interaction of graphene with the LDLR and ApoB protein was further evaluated using MM-PBSA calculations (Fig. 4). The binding free energy (ΔG Binding) for LDLR and graphene was calculated at − 18.53 kcal/mol, whereas the interaction with ApoB exhibited a significantly stronger binding free energy of − 64.35 kcal/mol. These findings suggest that ApoB has a much higher affinity for graphene compared to LDLR.

Structural dynamics analysis revealed that ApoB protein exhibited pronounced fluctuations, particularly in the flexible loop regions (residues PHE107, TYR111, and PHE390), which directly interact with the graphene surface. In contrast, LDLR demonstrated minimal structural fluctuations,

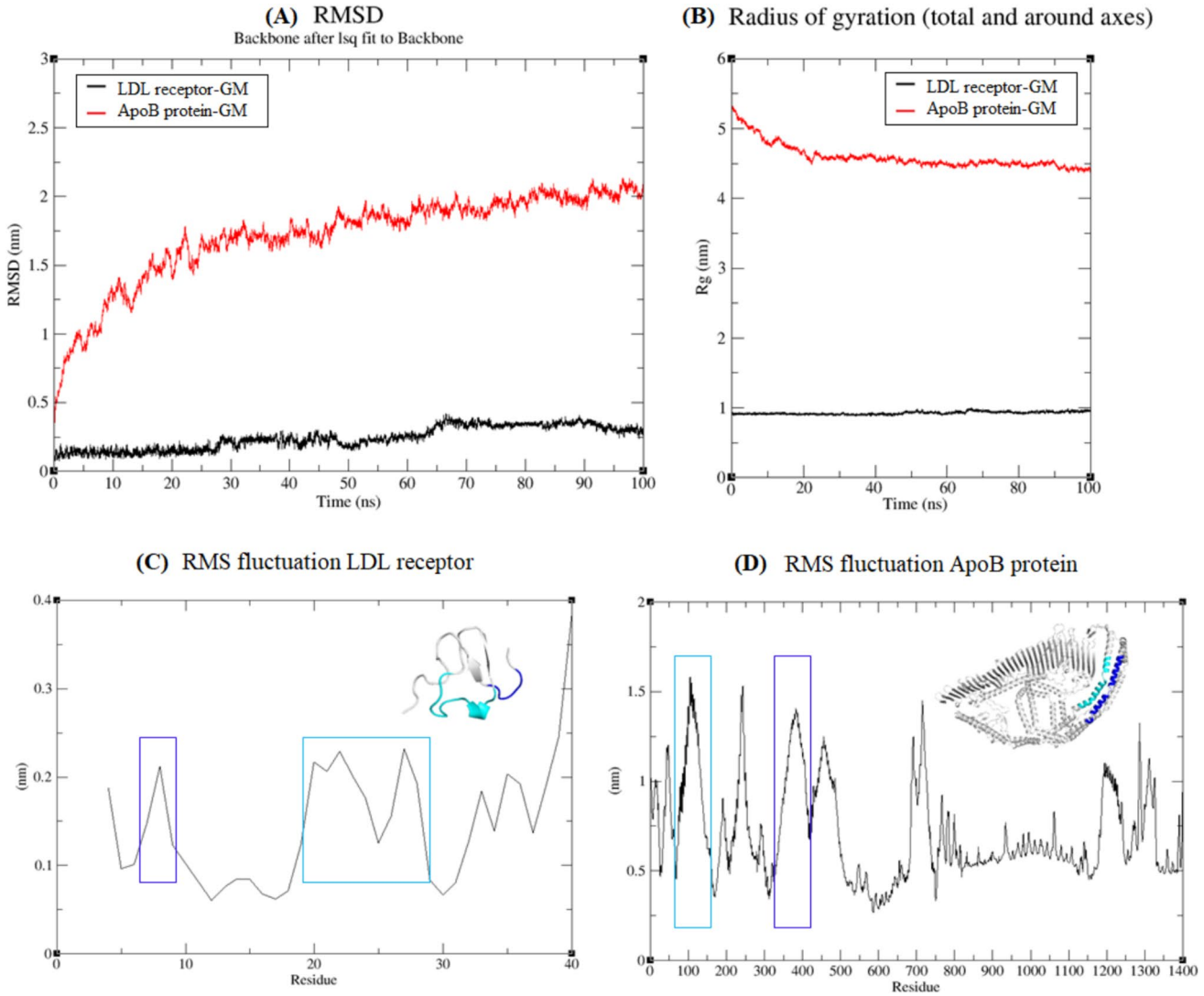

Fig. 3 Molecular dynamics analysis of LDLR and ApoB protein in complex with graphene. **A** RMSD: Time evolution of the RMSD for the backbone of the LDLR (black) and ApoB protein (red) when interacting with the graphene model (GM). The LDLR shows minimal deviation, indicating stability, while ApoB protein displays higher deviations due to its structural flexibility. **B** Compactness of the LDLR (black) and ApoB protein (red) over time. The LDLR maintains a stable Rg, indicating a compact and stable structure, whereas the ApoB protein shows fluctuations in Rg, consistent with its higher structural flexibility observed in the RMSD analysis. The stable Rg of the LDL receptor and the fluctuating Rg of the ApoB protein provide complementary support for the RMSD results, confirming relative stability and flexibility. **C** RMS Fluctuation of LDLR: Per-residue RMSF of the LDLR reveals regions of higher flexibility (highlighted in blue) corresponding to loop regions, while most of the structure remains stable. **D** RMSF of ApoB protein: Per-residue RMSF of the ApoB protein shows larger fluctuations (highlighted in blue), particularly in flexible regions such as loops and unstructured domains, indicating greater mobility compared to the LDL receptor

with binding interactions localized to residues HIS19 and TRP22. These differences highlight the stronger stability and interaction potential of graphene with ApoB compared to LDLR.

These findings align with the previously reported binding free energy results from Lat et al. [17], where graphene demonstrated strong binding affinities with other atherosclerosis-related receptors, particularly TLR4 (− 19.18 kcal/mol) and CD36 (− 18.39 kcal/mol). In contrast, positive binding free energy values were observed for interactions with SRA1 (378.19 kcal/mol) and LOX-1 (959.79 kcal/mol), indicating minimal or unfavorable interactions with these proteins. The dominant forces in graphene's binding with TLR4 and CD36 were hydrophobic interactions, whereas the binding to SRA1 involved cation-π interactions with LYS199.

Overall, the MM-PBSA results emphasize the preferential binding of graphene to ApoB, consistent with its role in modulating LDL metabolism, while also showing biologically relevant interactions with LDLR. This data further complements prior observations of graphene's selective interactions with atherosclerosis-related receptors, shedding light on its potential anti-atherogenic properties.

Characterization of Graphene Nanoplatelets

The Raman spectroscopy analysis of the synthesized GNPs, as shown in Fig. 5A, highlighted distinct spectral features that characterize its structural properties. The Raman spectrum exhibited a D band peak at 1278.46 cm^{-1} with an intensity of 5.17, a G band peak at 1569.34 cm^{-1} with an intensity of 21.25, and a 2D band peak at 2704.1 cm^{-1} with an intensity of 18.97. The intensity ratio of the D band to the G band (I_D/I_G) was calculated to be approximately 0.24, indicative of a relatively low degree of disorder in the graphene structure. This aligns with the high structural integrity of GNPs considered in our in silico simulations, ensuring comparable structural characteristics.

The XRD analysis of GNPs, depicted in Fig. 5B, revealed a prominent peak at a diffraction angle (2θ) of 26.475°, corresponding to the (002) plane of graphene. The calculated interlayer spacing (d-spacing) was approximately 0.34 nm (3.4 Å), confirming the crystalline nature of the synthesized GNPs. This structural feature is consistent with the models used in computational docking and molecular dynamics simulations, which rely on accurate representation of graphene's crystalline characteristics.

Furthermore, the FTIR analysis, as illustrated in Fig. 5C, revealed functional groups critical for interpreting the interaction of GNPs with biological targets. The spectrum exhibited a broad peak at 3434.78 cm^{-1}, corresponding to O–H stretching vibrations, suggesting the presence of hydroxyl groups. The peak at 2927.2 cm^{-1} corresponded to C–H stretching vibrations, while a distinct peak at 1631.91 cm^{-1} was attributed to C=C stretching vibrations, indicative of sp2 hybridized carbon atoms in the graphene lattice. Additionally, a peak at 1049.46 cm^{-1} was associated with C–O stretching vibrations, representing epoxy or ether groups, and a peak at 552.34 cm^{-1} could be attributed to out-of-plane bending vibrations of C–H bonds.

These structural and functional characteristics validate the suitability of the synthesized graphene for alignment with in silico studies. The consistent structural properties ensure that the GNPs used in computational modeling accurately represent the experimentally synthesized material, bridging the gap between computational predictions and experimental validation.

MMPBSA (kcal/mol)							
Receptor	**ΔG Binding**	**ΔE_VDW**	**ΔE_ELE**	**ΔG_POLAR**	**ΔG_NON POLAR**	**ΔGGAS**	**ΔGSOLV**
LDL receptor	-18.53	-28.88	-1.28	13.96	-2.33	-30.16	11.63
ApoB	-64.35	-72.17	-2.43	16.8	-6.55	-74.59	10.25

Fig. 4 Binding free energy analysis using MM-PBSA for LDL receptor and ApoB protein in interaction with the ligand. The table shows the decomposition of the total binding energy (ΔG Binding) into van der Waals energy (ΔE_VDW), electrostatic energy (ΔE_ELE), polar solvation energy (ΔG_POLAR), and non-polar solvation energy (ΔG_NON POLAR). The total gas-phase energy (ΔG_GAS) and solvation energy (ΔG_SOLV) are also presented, highlighting the significant contribution of van der Waals interactions to the binding affinity

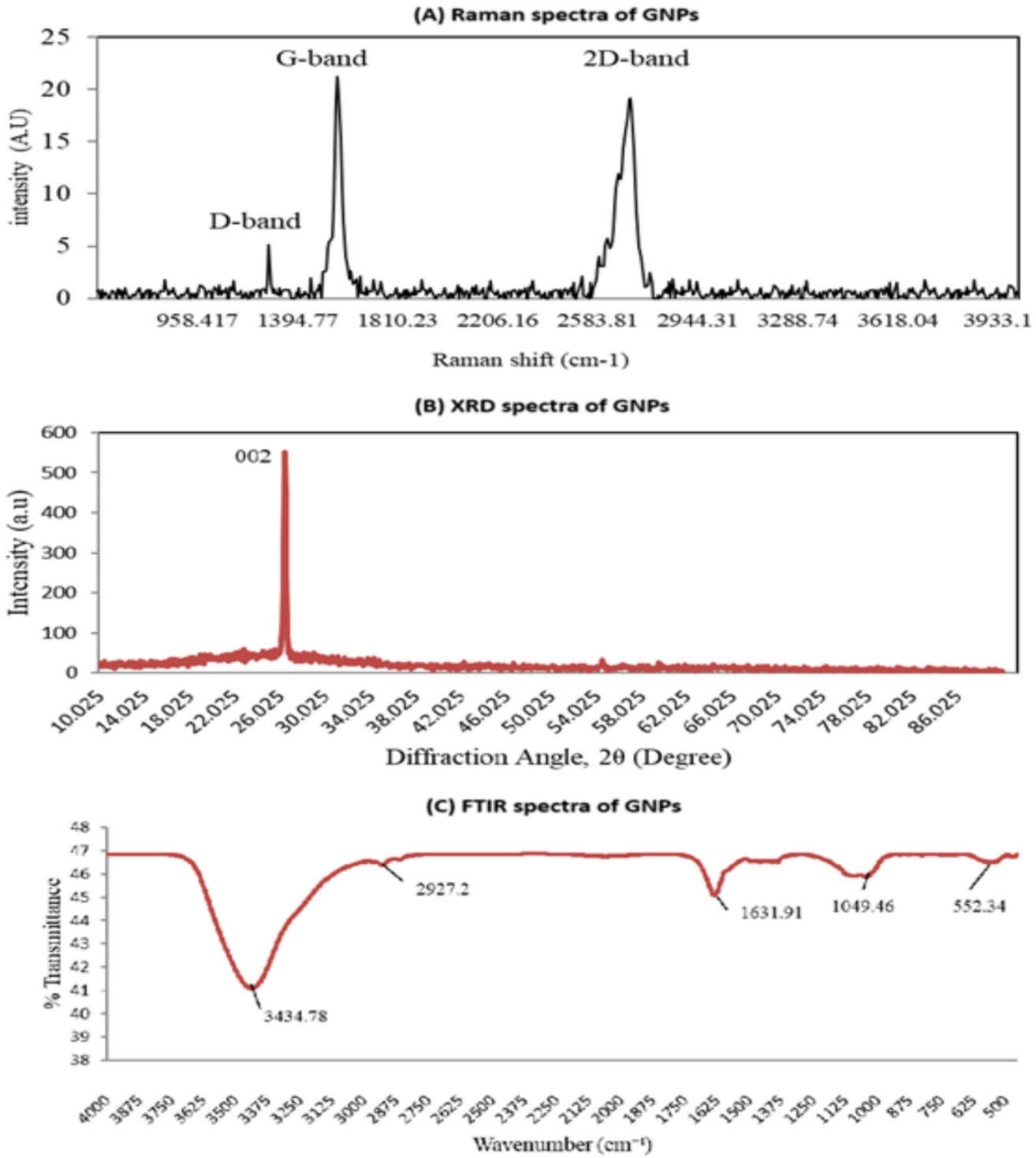

Fig. 5 Characterisation of GNPs. **A** Raman spectrum GNPs highlighting the D-band, G-band, and 2D-band, indicative of graphitic structures and defects. **B** XRD spectrum of GNPs showing a prominent (002) peak, confirming the crystalline nature of graphene. **C** FTIR spectrum of GNPs indicating surface-associated functional groups commonly observed in graphene nanoplatelets, without compromising structural stability

Cell Viability of RAW264.7 Cells Treated with Graphene Nanoplatelets

The cell viability of RAW264.7 macrophages treated with varying concentrations of GNPs for 24, 48, and 72 h is shown in Fig. 6. At 24 h, GNPs at concentrations between 0.1 and 1 µg/mL reduced cell proliferation by approximately 5%, while at 48 h, this reduction increased to 10%. At higher concentrations (5–50 µg/mL), a more significant decrease in cell proliferation was observed, with reductions exceeding 15% at 24, 48, and 72 h. Based on these results, the concentration of 1 µg/mL was selected for further downstream experiments, as it exhibited minimal cytotoxicity while still demonstrating a measurable impact on cell viability.

Lipid Droplet Accumulation in RAW264.7 Cells Treated with oxLDL, GNPs, and Their Combination

Lipid droplet accumulation in RAW264.7 macrophages treated with oxLDL, GNPs, and their combination was assessed using Oil Red O staining and visualized under a microscope (Fig. 7A–D). Lipid droplets appeared as red-stained structures in the cytoplasm, while cell nuclei were counterstained blue. In untreated and GNP-treated RAW264.7 cells, minimal lipid droplet accumulation was observed at both 24 and 48 h (Fig. 7A and C). In contrast, prominent lipid droplet accumulation was detected in the cytoplasm of cells treated with oxLDL alone at both time points, indicating foam cell formation (Fig. 7B). Notably, co-treatment with GNPs markedly reduced lipid droplet accumulation in oxLDL-treated RAW264.7 cells (Fig. 7D). This inhibitory effect was more pronounced at 48 hours compared to 24 h, suggesting a time-dependent protective effect of GNPs against oxLDL-induced lipid accumulation.

To quantitatively support these observations, Oil Red O staining was analyzed using ImageJ software by measuring the percentage of Oil Red O–positive area (Fig. 7E). Quantitative analysis confirmed that oxLDL treatment significantly increased lipid accumulation compared to untreated controls at both 24 and 48 h ($P < 0.05$). Co-treatment with GNPs significantly reduced the Oil Red O–positive area relative to oxLDL-treated cells ($P < 0.05$), with a greater reduction observed at 48 hours. Data are presented as mean ± SD from three independent experiments ($n = 3$), corroborating the qualitative staining results.

Total Cholesterol Content in Treated RAW264.7 Cells

The formation of macrophage-derived foam cells is closely linked to increased total cholesterol levels in macrophages. To complement the microscopic visualization of lipid droplets, total cholesterol content was quantified in RAW264.7 cells treated with oxLDL, GNPs, and their combination at 24 and 48 h (Fig. 8). GNPs alone slightly increased total cholesterol compared to untreated cells, but the increase was markedly lower than that caused by oxLDL. Co-treatment of oxLDL with GNPs significantly reduced cholesterol accumulation compared to oxLDL alone. RAW264.7 macrophages treated with oxLDL exhibited significantly elevated total cholesterol levels compared to untreated cells, GNP-treated cells, and those co-treated with oxLDL and GNPs at both 24 and 48 h ($P < 0.001$ and $P < 0.0001$, respectively). Notably, the addition of GNPs to oxLDL-treated RAW264.7 cells significantly reduced total cholesterol content at both time points compared to cells treated with oxLDL alone ($P < 0.001$ and $P < 0.0001$). This reduction indicates the potential of GNPs to inhibit oxLDL-induced cholesterol accumulation in macrophages.

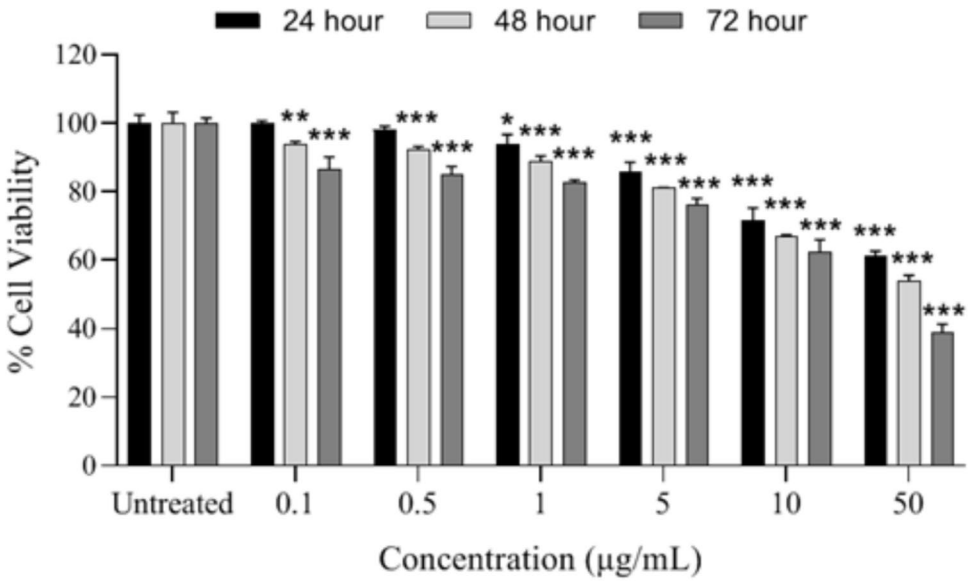

Fig. 6 Cell viability of RAW264.7 cells treated with different concentrations of GNPs (0.1–50 µg/ml) at 24, 48, and 72 h. Cell viability decreases significantly in a dose-dependent and time-dependent manner, especially at higher concentrations (10–50 µg/mL) and longer incubation periods. The cell viability percentage were compared between the untreated group vs. treated groups (*$P < 0.05$). The values represent the mean ± SD. The experiment was performed three times ($n = 3$)

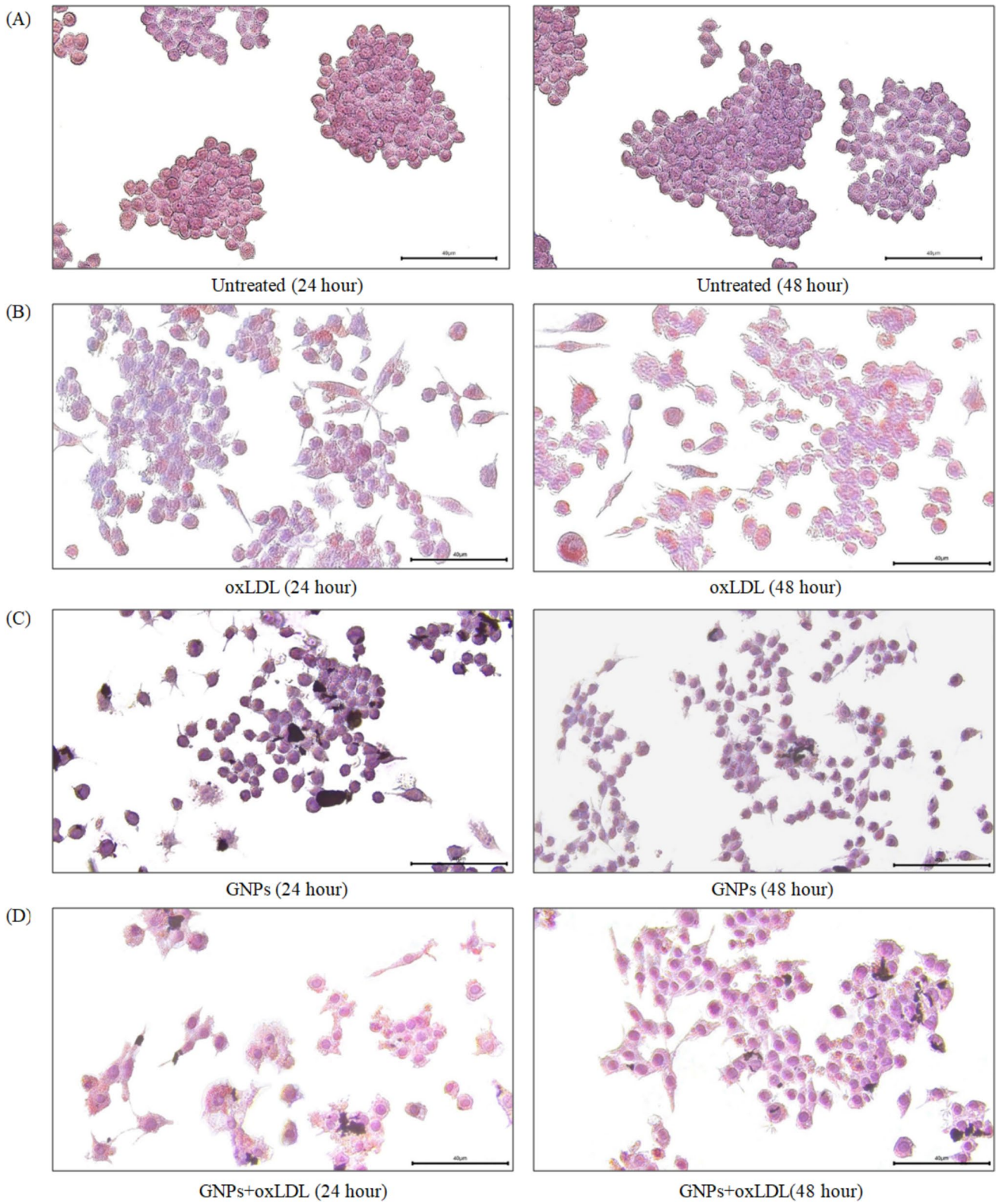

Fig. 7 GNPs hinder accumulation of lipid droplets in the cytoplasm of oxLDL-treated RAW264.7 cells. Untreated RAW264.7 cells (**A**), OxLDL-treated RAW264.7 cells (**B**), GNPs-treated RAW264.7 cells (**C**), GNPs and oxLDL-treated RAW264.7 (**D**), were cultured for 24 and 48 h. In oxLDL-treated cells (**B**), a significant accumulation of red-stained lipid droplets is observed, indicating foam cell formation. In contrast, GNP treatment in combination with oxLDL (**D**) reduced lipid droplet accumulation, with a greater reduction observed at 48 h compared to 24 h. The treated RAW264.7 macrophages were visualized under microscope at 40× magnification after undergone ORO staining at each treatment time. **E** Quantification of Oil Red O-positive area (%) was performed using ImageJ software. Data are presented as mean ± SD from three independent experiments (n = 3). Scale bar = 40 µm

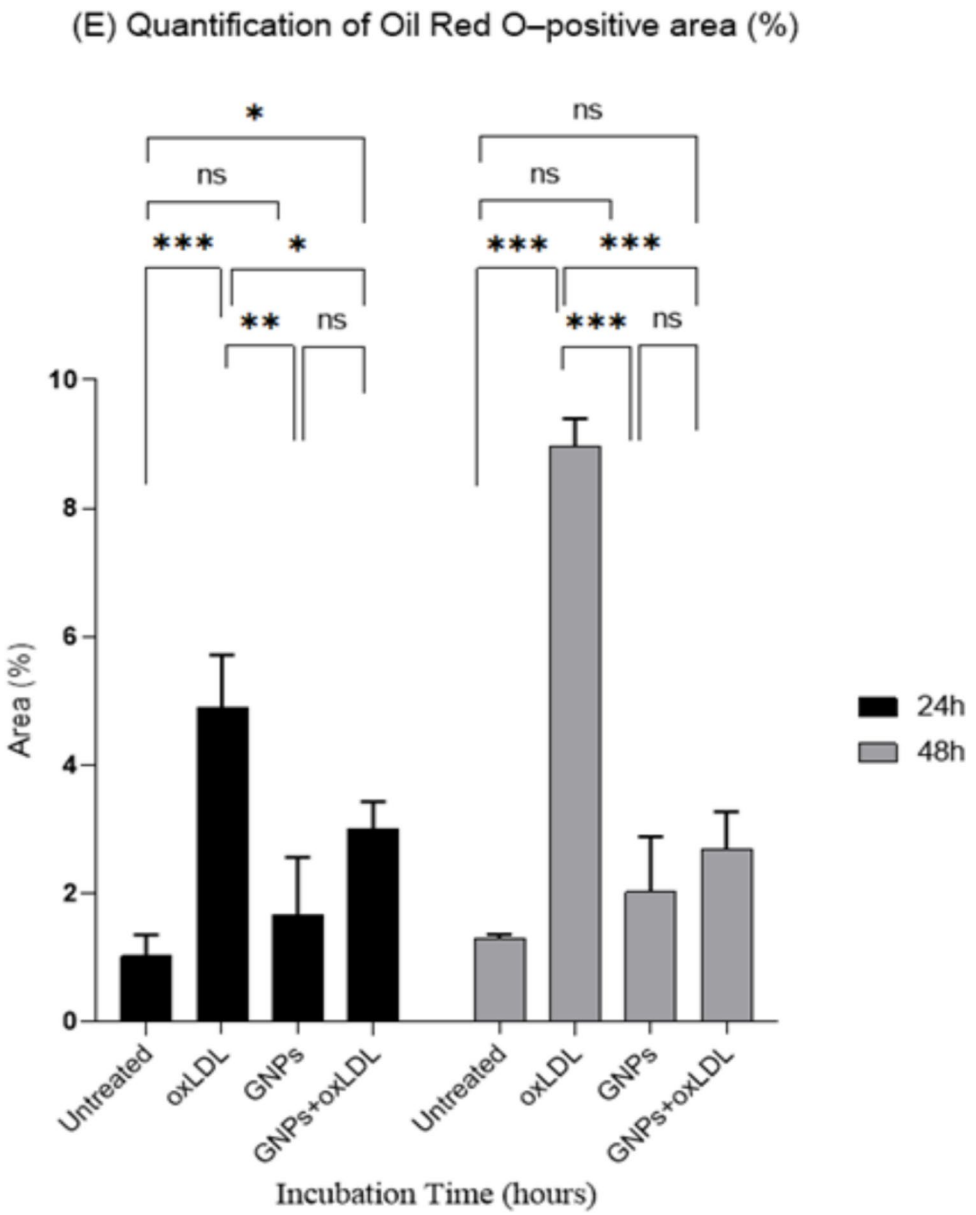

Fig. 7 (continued)

Cytokine Secretion in Treated RAW264.7 Cells

The pro-inflammatory cytokines IFNγ, TNFα, IL-1β, and IL-6 were quantified in the supernatant of RAW264.7 macrophages treated with oxLDL, GNPs, and their combination at 48 hours (Fig. 9A–D). RAW264.7 cells treated with oxLDL exhibited significantly higher levels of IFNγ, TNFα, IL-1β, and IL-6 compared to untreated cells ($P < 0.05$, $P < 0.0001$, respectively). This elevation highlights the pro-inflammatory response induced by oxLDL in macrophages. Treatment with GNPs alone resulted in increased levels of IFNγ, TNFα, IL-1β, and IL-6 relative to untreated cells. However, the elevations in IFNγ and TNFα were not statistically significant, whereas IL-1β and IL-6 were significantly increased. Notably, IL-6 secretion in the GNP-only group was higher than that observed in oxLDL-treated cells. In contrast, co-treatment with GNPs and oxLDL resulted in lower levels of IFNγ, TNFα, and IL-1β compared to oxLDL treatment alone. The addition of GNPs to oxLDL-treated macrophages significantly reduced the secretion of IFNγ, IL-1β, and IL-6 compared to oxLDL-treated cells ($P < 0.05$, $P < 0.0001$, $P < 0.0001$, respectively, Fig. 9A, C, and D). However, GNPs did not significantly alter TNFα levels in the supernatant of oxLDL-treated macrophages, as shown in Fig. 9B. These results suggest that GNPs possess an anti-inflammatory effect by modulating specific cytokines,

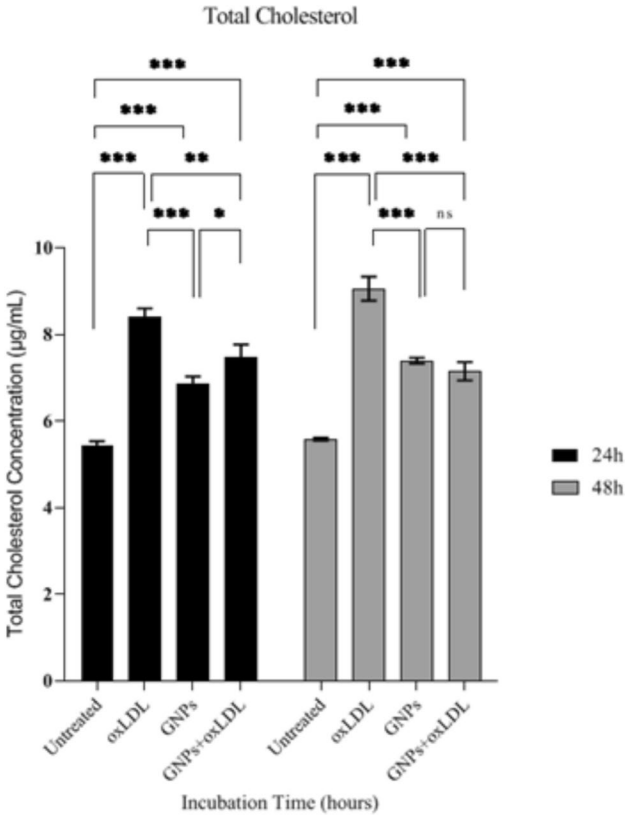

Fig. 8 GNPs reduced total cholesterol contents in oxLDL-treated RAW264.7 cells. Untreated and treated RAW264.7 cells at 24 and 48 h were lysed in RIPA buffer and measured total cholesterol using a commercial kit. Values are expressed as mean ± SD from three independent experiments (n = 3). *P < 0.05 compared to oxLDL group vs. combination of oxLDL + GNPs treated groups

potentially mitigating the inflammatory environment created by oxLDL in macrophages.

Gene Expression Analysis of Treated RAW264.7 Cells

Gene expression levels of IL-1β, ABCA-1, ACAT-1, and CD36 were analyzed in RAW264.7 macrophages treated with oxLDL, GNPs, and their combination for 48 hours (Fig. 10A–D). RAW264.7 cells treated with oxLDL exhibited significantly higher expression of IL-1β,ACAT-1, and CD36 compared to untreated cells ($P < 0.0001$), indicating an inflammatory and pro-atherogenic response (Fig. 10A, C, and D). Conversely, the expression of ABCA-1, a key regulator of cholesterol efflux, was markedly lower in oxLDL-treated macrophages (Fig. 10B). The addition of GNPs significantly reduced the expression of IL-1β, ACAT-1, and CD36 in oxLDL-treated RAW264.7 cells ($P < 0.0001$), suggesting the ability of GNPs to counteract the inflammatory and pro-foam cell gene profile induced by oxLDL (Fig. 10A, C, and D). On the other hand, GNPs significantly upregulated ABCA-1 gene expression in oxLDL-treated cells compared to oxLDL treatment alone ($P < 0.0001$, Fig. 10B), highlighting a potential enhancement of cholesterol efflux. These findings indicate that GNPs modulate the expression of genes involved in inflammation, lipid metabolism, and foam cell formation, aligning with their anti-atherogenic potential demonstrated in other experimental contexts.

Discussion

The current study aimed to investigate the interactions between GNPs and atherosclerosis-related proteins, along with their potential effects on macrophage-derived foam cell formation. This was achieved through a combination of in silico molecular dynamics simulations and experimental in vitro assays. The integration of both approaches provides valuable insights into the mechanisms by which GNPs may modulate the pathophysiology of atherosclerosis.

Molecular Docking and Interaction Analysis

This molecular docking study reveals that graphene exhibits a stronger binding affinity for ApoB compared to LDLR. The higher binding affinity for ApoB indicates graphene's preference for interacting with a key structural protein in LDL, which plays a central role in lipid metabolism and atherosclerosis development [29]. Our prior computational studies demonstrated that pristine graphene exhibits strong binding affinities with atherosclerosis-related receptors, particularly TLR4 (− 13.3 kcal/mol), followed by LOX1 (− 11.3 kcal/mol), SRA1 (− 11.2 kcal/mol), and CD36 (− 10.7 kcal/mol) [17]. In this study, molecular docking and dynamics simulations were performed using the full-length LDL receptor (LDLR) and ApoB-100, encompassing all functional domains relevant to LDL recognition, uptake, and macrophage foam cell formation. While these proteins are central to foam cell biology, it is acknowledged that additional receptors, such as LDL receptor-related protein 1 (LRP1), as well as modified LDL components or other apolipoproteins, may also influence lipid uptake and inflammatory signaling. LRP1, a member of the LDLR family, has been shown to mediate the uptake of aggregated lipoproteins and contribute to macrophage foam cell formation, indicating that multiple receptor–ligand interactions beyond LDLR–ApoB-100 are relevant in foam cell biology [31]. Furthermore, macrophage scavenger receptors such as CD36 and class A scavenger receptor (SR-A) have been demonstrated to facilitate uptake of oxidized and modified LDL species, and their roles may overlap or compensate beyond the classical LDLR–ApoB-100 pathway, highlighting the complexity and redundancy of receptor–ligand interactions in foam cell formation [32]. Future studies incorporating these additional receptors and ligands could further refine

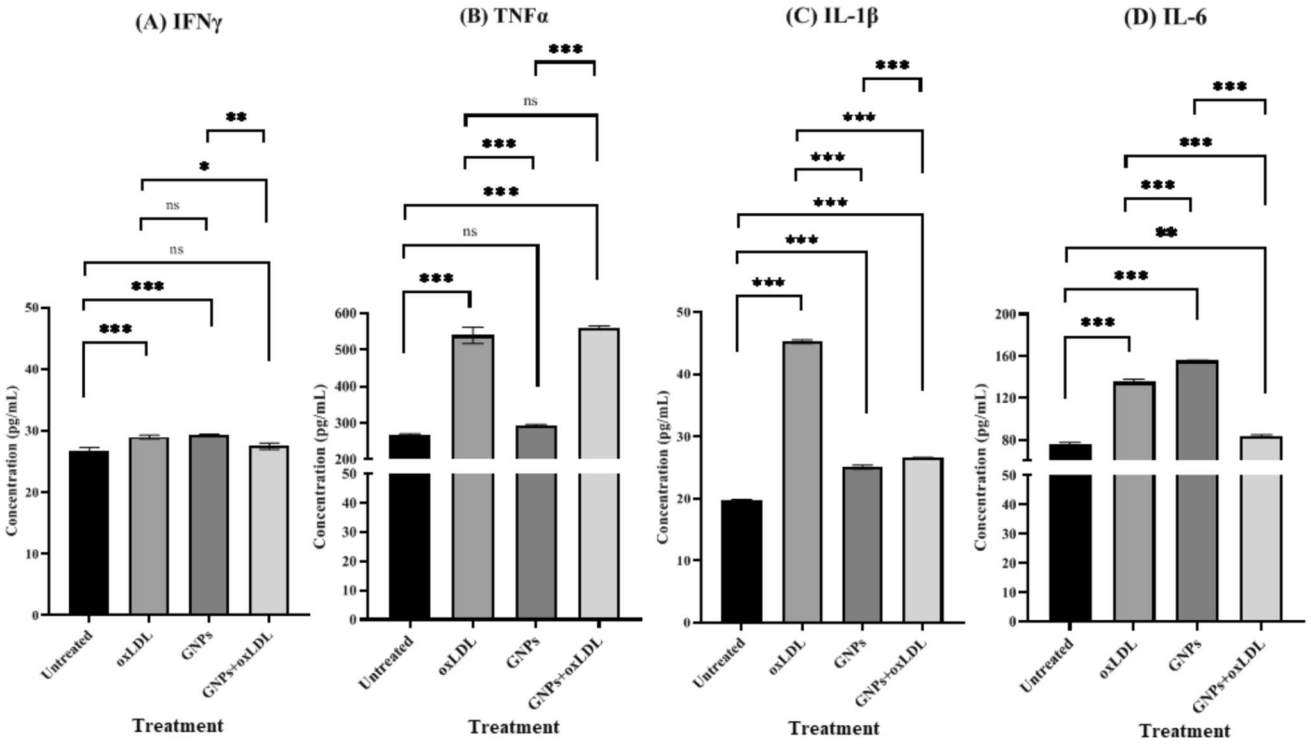

Fig. 9 GNPs reduced IFNɣ, IL-1β and IL-6 secretions in the supernatant of oxLDL-treated RAW264.7 cells. The level of IFNɣ (**A**), TNFα (**B**), IL-1β (**C**) and IL-6 (**D**) secreted in the supernatant of untreated and treated RAW264.7 cells at 48 h were measured using ELISA kit. Values are expressed as mean ± SD from three independent experiments (n = 3). *P < 0.05 compared to oxLDL group vs. combination of oxLDL + GNPs treated groups

our understanding of GNP effects in the context of foam cell formation. The interaction between graphene and ApoB, marked by π-stacking interactions with TYR111, PHE107, and PHE390, likely disrupts LDL functionality, affecting lipid homeostasis and potentially promoting foam cell formation, a hallmark of atherogenesis [29]. Although graphene's binding to LDLR is moderate, its binding remains significant given the receptor's essential role in LDL uptake and clearance [30]. This suggests that graphene could modulate lipid metabolism and influence atherosclerosis progression.

The interaction analysis highlights key structural insights into graphene's binding mechanisms. For LDLR, T-stacking interactions with TRP22 and HIS19, and cation-π interactions with HIS19, emphasize the role of aromatic and hydrophobic interactions in stabilizing these interactions [33, 34]. Similarly, in ApoB, π-stacking interactions dominate the binding process, reflecting the role of aromatic residues in lipid metabolism [33–35]. Prior studies also noted specific interaction patterns between graphene and LOX1, including cation-π interactions with ARG-208 and π-stacking interactions with TRP-215, further emphasizing the critical role of such non-covalent forces in molecular recognition [17].

RMSD, Rg, RMSF and Structural Adjustments

Lower RMSD and Rg values observed for LDLR suggest a more compact structure with limited conformational changes, reflecting its smaller size and fewer interaction sites [36, 37]. This compactness is consistent with findings on SRA1, where lower RMSD (0.199 nm) and Rg (1.688 nm) values indicate structural stability [17]. In contrast, ApoB exhibits higher RMSD and Rg values due to its extended structure, facilitating dynamic interactions with graphene. For instance, TLR4 showed the highest Rg values (3.114 nm) when interacting with graphene, highlighting its flexibility [17]. These dynamics underscore that proteins like ApoB, with greater flexibility and surface area, form more stable and multifaceted interactions with graphene compared to compact proteins like LDLR or SRA1 [36, 37]. Similar trends are seen in PON1, where reduced Rg reflects structural compactness, enhancing stability and interactions [38], and in SIRT1, where RMSD and Rg values highlight the role of flexibility in binding mechanisms and functional adaptability [39, 40]. RMSF analysis further reveals that structural adjustments in flexible and aromatic residue-rich regions of LDLR and ApoB contribute to binding stability through hydrophobic effects and π-π stacking [41].

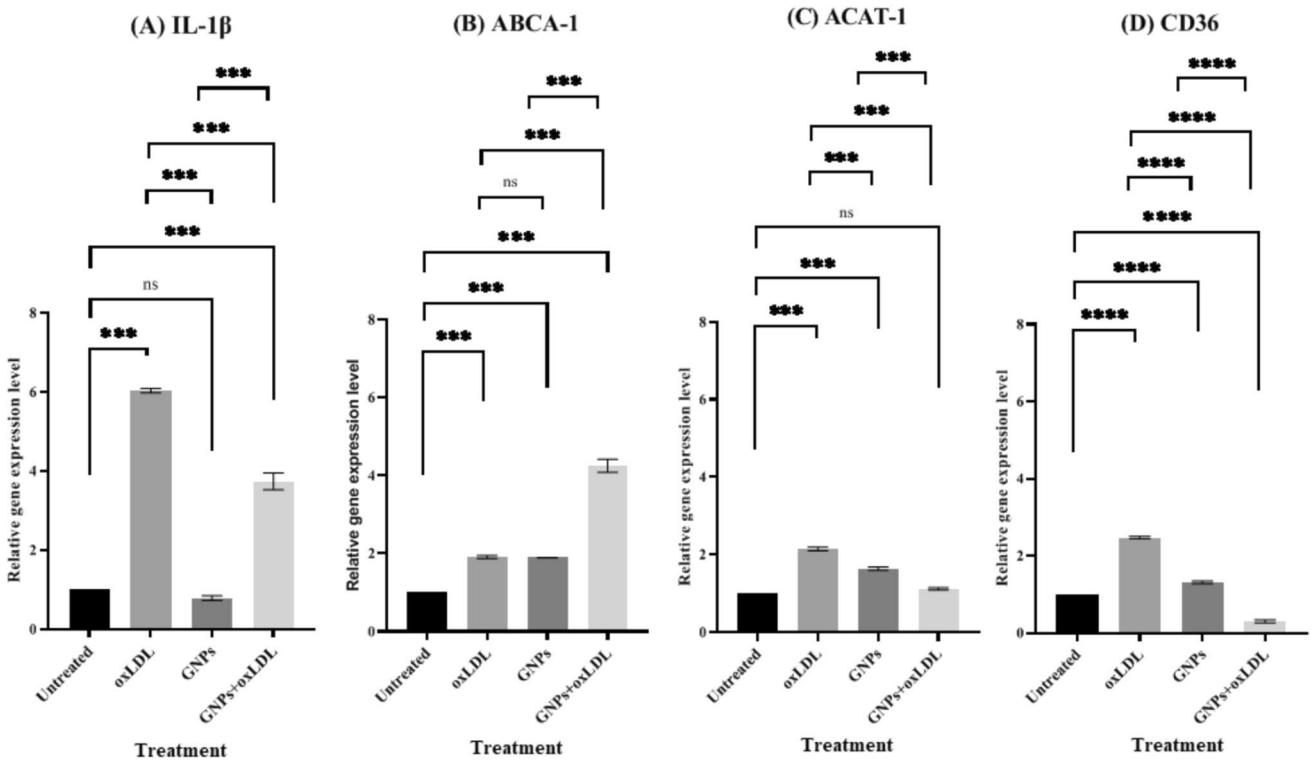

Fig. 10 GNPs down regulated IL-1β, ACAT-1 and CD36 genes but augment ABCA-1 gene expression in oxLDL-treated RAW264.7 cells. Total RNA was extracted from untreated and treated RAW264.7 cells at 48 hours and was synthesized into cDNA. IL-1β (**A**), ABCA-1 (**B**), ACAT-1 (**C**) and CD36 (**D**) genes expression were quantitated using qRT-PCR. Values are expressed as mean ± SD from three independent experiments (n = 3). ****P < 0.001 compared to oxLDL group vs. combination of oxLDL + GNPs treated groups

MM-PBSA and Binding Affinity

MM-PBSA calculations confirm graphene's stronger binding affinity for ApoB compared to LDLR, attributed to ApoB's larger surface area and ability to form multiple interaction points [41]. Previously, we reported high binding energies of graphene with TLR4 (− 19.18 kcal/mol) and CD36 (− 18.39 kcal/mol), while interactions with SRA1 and LOX1 showed positive free energy values [17]. This highlights graphene's reliance on hydrophobic and π-interactions for binding stability, as observed with ApoB. In contrast, the moderate binding affinity of graphene for LDLR suggests limited potential to directly interfere with LDL uptake and clearance [42]. The smaller graphene models employed in this study, though restricting the number of interaction sites, provide a computationally efficient representation of graphene's hydrophobic properties and their influence on binding behaviors [43, 44]. These findings emphasize the critical role of graphene's size, shape, and surface properties in determining binding dynamics.Future investigations should focus on protein interactions with functionalized graphene surfaces to better understand the impact of surface chemistry on binding stability and protein behavior.

Structural Quality and Functional Group Analysis

In our study, the distinct 2D band in Raman spectroscopy, along with XRD and FTIR, confirms that the commercial GNPs used in this study exhibit high structural quality with minimal defects and preserved graphene layers. The FTIR analysis also reveals that the GNPs retain several oxygen-containing functional groups, likely due to partial oxidation or functionalization during production, as well as exposure to environmental moisture and air [45]. The FTIR analysis of the GNPs in this study aligns with findings by Firdaus et al. who reported that sulfonitric treatments using H_2SO_4 and HNO_3 introduce oxygen-containing functional groups such as hydroxyl (–OH), carbonyl (C=O), and carboxyl (–COOH) [45]. These modifications enhance the hydrophilicity and dispersibility of GNPs in polar solvents [45]. Similarly, in our study, the observed functional groups likely result from residual oxidation during synthesis or exposure to environmental moisture and air, as evidenced by the O–H stretching (~3400 cm^{-1}) and C=O stretching (~1720 cm^{-1}) peaks in the FTIR spectra.

In the current study, the distinct 2D band in Raman spectroscopy, along with XRD and FTIR, confirms that the commercial GNPs used in this study exhibit high structural

quality with minimal defects and preserved graphene layers. Although this study does not specifically investigate the stability or aggregation behaviour of GNPs in biological media, prior studies have shown that functionalized graphene derivatives exhibit improved dispersibility and reduced toxicity. Future studies should explore the behaviour of GNPs in biological environments to better understand their stability and long-term effects.

Inhibition of Foam Cell Formation

The effect of GNPs on foam cell formation was investigated by treating RAW264.7 murine macrophage cells with oxLDL, GNPs, or a combination of both for 24 and 48 h. The concentration of GNPs and treatment duration were optimized using cell viability assays. GNPs were administered concurrently with oxLDL. This design allows assessment of GNPs' ability to inhibit foam cell formation during lipid uptake, rather than reversing established lipid accumulation. Lipid droplets in treated cells were visualized using Oil Red O staining, a standard technique for assessing foam cell formation [46]. Microscopic analysis showed a substantial accumulation of lipid droplets in oxLDL-treated RAW264.7 cells, indicating successful foam cell formation. In contrast, treatment with GNPs significantly reduced lipid droplet accumulation in a time-dependent manner, suggesting that GNPs inhibit foam cell formation. This observation was supported by quantifying total cholesterol content, which was markedly higher in oxLDL-treated cells but significantly reduced by GNPs treatment. Previous research indicates that GNPs can extract cholesterol from cell membranes due to their porous structure and strong surface adhesion, thereby reducing cholesterol aggregation in lysosomes [47, 48]. Additionally, another graphene-based nanomaterial, namely GO, has been shown to reduce lipid content in THP-1 macrophages [49] and endothelial cells [50]. Furthermore, GO has been found to modify lipid profiles in vascular smooth muscle cells [51] and 3D human brain organoids [52].

Modulation of Inflammatory Cytokines

Further investigation into the mechanisms underlying GNPs' effects revealed that they modulate several key inflammatory cytokines associated with foam cell formation. ELISA results demonstrated elevated levels of IFNγ, TNFα, IL-1β, and IL-6 in the supernatants of oxLDL-treated RAW264.7 cells. GNPs treatment significantly decreased the secretion of IFNγ, IL-1β, and IL-6. These cytokines are crucial in atherosclerosis; for example, IFNγ affects cholesterol metabolism by modulating the expression of genes such as ApoE, ABCA-1, and ACAT-1 [53, 54]. Elevated IFNγ can reduce cholesterol efflux and promote foam cell formation, while GNPs' ability to inhibit IFNγ secretion could thus reduce cholesterol accumulation. Similarly, IL-1β, which is activated through the NLRP3 inflammasome and scavenger receptor CD36, promotes foam cell formation [55]. IL-6, another key cytokine associated with atherosclerosis, was also found to be elevated in oxLDL-treated cells. IL-6's role in promoting foam cell formation involves increasing the expression of scavenger receptors like CD36 and SRA [56]. GNPs may decrease the secretion of IFNγ, IL-1β, and IL-6 by inhibiting NF-κB, which normally binds to the promoter regions of these genes. This inhibition prevents NF-κB from initiating the transcription of various proinflammatory genes and the subsequent release of proinflammatory factors [57]. A recent study demonstrated that GNPs effectively and rapidly remove cytokines from human plasma spiked with a cytokine cocktail [58]. Within just 5 minutes of direct contact, the concentration of smaller cytokines, IL-8 (8 kDa) and IL-1β (17 kDa), was reduced from over 1500 pg/mL to 20 pg/mL. In comparison, the removal of larger cytokines, IL-10 (18.5 kDa) and IL-6 (20.5 kDa), was somewhat slower, but GNPs still achieved 60 and 50% removal, respectively, within the same time frame [58]. This rapid adsorption can be attributed to the complete accessibility of the GNPs surface and minimal diffusion barriers [58]. These findings highlight the potential of GNPs for the efficient removal of a broad spectrum of pro-atherogenic cytokines, which could contribute to the inhibition of atherosclerotic plaque development.

Gene Expression Modulation

The study also investigated the impact of GNPs on gene expression related to cholesterol metabolism. Notably, GNPs were found to decrease the expression of pro-atherogenic genes such as IL-1β and CD36, while increasing the expression of ABCA-1, which is crucial for cholesterol efflux [59]. Additionally, GNPs downregulated ACAT-1, an enzyme involved in cholesterol esterification and foam cell formation [60]. The increased ABCA-1 expression indicates enhanced cholesterol efflux and reduced foam cell formation, which aligns with previous findings that ABCA-1 not only promotes lipid removal but also exerts anti-inflammatory effects [59].

The downregulation of CD36 observed in GNP-treated macrophages suggests that GNPs may interfere with CD36-mediated pathways, potentially mimicking or competing with oxLDL, altering receptor conformation, or modulating downstream signalling [61]. Previous studies have demonstrated that ligand-coated nanoparticles preferentially accumulate in plaque macrophages via CD36, reducing lipid uptake and attenuating foam cell formation and inflammatory signaling [62]. Amphiphilic core/shell nanoparticles similarly bind to CD36 and SRA, downregulate receptor expression, and suppress oxLDL uptake in macrophages,

emphasizing the role of nanoparticle design in modulating receptor-mediated pathways [63]. Furthermore, EGCG-loaded nanoparticles targeting CD36 have been reported to reduce oxLDL uptake, decrease CD36 expression, and inhibit downstream inflammatory signaling in plaque macrophages [64]. Together, these studies suggest that the down-regulation of CD36 observed in GNP-treated macrophages in our study may result from competitive binding with oxLDL, modulation of receptor conformation, or interference with downstream signaling, thereby reducing lipid accumulation and pro-inflammatory responses. This provides a plausible mechanism by which GNPs may elicit effects similar to the native ligand of CD36, ultimately attenuating foam cell formation and atherogenic inflammation.

The only related study focused on large-sized graphene oxide (GO-L), which was shown to inhibit lipid metabolism in THP-1 macrophages via the peroxisome proliferator-activated receptor (PPAR) pathway [49]. Recently, various nanomaterials have been engineered to enhance cholesterol efflux, reduce inflammation, and improve outcomes in atherosclerosis. For instance, HA-Fc/NP3ST, a nano-module combining disc-shaped HDL and hyaluronic acid-ferrocene conjugates, demonstrated ROS-responsive size reduction, targeting cholesterol efflux in macrophages and reducing plaque and lipid deposition in mice [65]. Similarly, MnO2-curcumin nano-drugs reprogram macrophages from the M1 to M2 phenotype, inhibit HIF-1α, and restore lipid efflux, effectively reducing foam cell formation [66]. Another nanoprobe, integrating hyaluronic acid and porphyrin onto black TiO2, targets foam cells in plaques, modulating the SREBP2/LDLR pathway to reduce cholesterol uptake and enhance ABCA1-mediated efflux without causing excessive apoptosis or necrosis [66].

Size-Dependent Biological Effects of GNPs

The size of GNPs is a critical factor influencing their biological effects, as evidenced by both in silico and in vitro studies. Molecular Docking and MD simulations have shown that smaller GNPs exhibit enhanced interactions due to their higher surface-to-volume ratio, enabling stronger protein binding and cellular interactions [17]. These computational findings are consistent with the biological responses observed in this study, including the inhibition of foam cell formation and the modulation of cytokine secretion.

Although the size of GNPs was not directly measured in this in vitro study, existing literature supports the pivotal role of size in determining biological activity [67, 68]. Computational studies predict that smaller GNPs, with their higher surface-to-volume ratio, demonstrate stronger binding affinities and more stable interactions with cellular proteins and membranes [69, 70]. These enhanced interactions promote increased cellular uptake and modulate pathways related to lipid metabolism and inflammation, providing a mechanistic explanation for their observed biological effects. MD simulations further emphasize the stability and affinity of these interactions, shedding light on their dynamic nature [70]. Smaller GNPs are particularly effective in regulating cholesterol content, gene expression, and inflammatory responses, owing to their superior penetration capabilities and reactivity [67]. Conversely, larger GNPs exhibit reduced binding efficiency and a tendency for aggregation, which diminishes their biological activity [68, 69].

The integration of in silico and in vitro approaches highlights the significance of GNP size in determining their efficacy. Computational tools provide mechanistic insights into the size-dependent molecular interactions, while experimental data validate these outcomes. Together, these findings reinforce the importance of GNPs size in shaping their biological effects, offering valuable guidance for their development in targeted therapeutic applications.

Nanoparticle Strategy and Prospects for Atherosclerosis Therapy

GNPs have emerged as a promising nanomaterial for atherosclerosis therapy due to their distinctive physicochemical characteristics. They possess a large surface area, strong mechanical stability, and the ability to interact with biomolecules such as apolipoprotein B and low-density lipoprotein receptor. Unlike polymeric or other non-metallic nanoparticles, GNPs may produce biological effects without requiring encapsulated drugs or synthetic targeting ligands, which could simplify formulation and reduce unintended interactions. Studies involving LDL-based nanoparticles have demonstrated that ApoB present on the particle surface enables preferential accumulation in atherosclerotic plaques and uptake by intimal macrophages through LDLR and SRs such as CD36 and SR-A. These interactions allow modulation of foam cell formation, cholesterol transport, and inflammatory signaling without additional surface modification [11, 12]. Similarly, polymeric nanoparticles, including PLGA carriers loaded with Liver X receptor agonists, have been shown to enhance cholesterol efflux and suppress macrophage inflammation both in vitro and in vivo, although these systems require more complex drug-loading procedures [9, 10]. High-throughput investigations using HDL-mimicking nanoparticles have further highlighted that properties such as size, composition, and surface chemistry are critical for achieving selective macrophage targeting and accumulation in plaques. Taken together, these findings suggest that GNPs, based on their inherent physicochemical

properties, may interact with ApoB, LDLR, and scavenger receptors such as CD36, reduce foam cell formation, and regulate inflammatory responses. While the current study focuses on in silico and in vitro analyses, the translational potential of GNPs is supported by in vivo evidence from LDL- and HDL-mimicking nanoparticles that accumulate in plaques and target macrophages. Future research should evaluate in vivo biodistribution, long-term biocompatibility, and systemic safety to confirm the clinical applicability of GNPs.

Influence of Human Serum Albumin and Protein Corona on GNP Therapeutic Performance

The current study explored the potential of GNPs as a therapeutic strategy to mitigate atherosclerosis by targeting foam cell formation. The results demonstrate that GNPs exhibit strong interactions with LDLR and ApoB, reduce intracellular lipid accumulation, and modulate inflammatory gene expression in macrophages. These findings provide mechanistic insight into the anti-atherogenic effects of GNPs and set the stage to consider how physiological factors, such as interactions with blood proteins, may influence their therapeutic performance. GNPs introduced into biological environments are rapidly coated by plasma proteins, forming a dynamic protein corona that can profoundly influence nanoparticle surface properties, biological identity, and interactions with target molecules [71, 72]. Human serum albumin (HSA), the most abundant plasma protein, preferentially adsorbs onto graphene-based nanomaterials, rendering them surface active and altering interactions with lipid interfaces and membrane-associated proteins [72, 73]. This adsorption may modify the accessibility of GNPs to lipid-associated targets, such as LDLR and ApoB, potentially influencing lipid uptake, foam cell formation, and inflammatory signaling. Recent reviews have highlighted that protein corona formation on graphene oxide and related nanomaterials alters surface chemistry, charge, and hydrophobicity, thereby modulating cellular uptake, biodistribution, and therapeutic specificity [74]. Furthermore, experimental studies have shown that HSA binding can induce conformational changes in the adsorbed protein, which may further influence nanoparticle interactions with biological targets [72, 73]. Taken together, these findings underscore the importance of considering albumin and other plasma proteins when evaluating the therapeutic potential of GNPs, as protein corona formation may modulate both their targeting efficiency and biological activity under physiological conditions.

Limitations of the Study and Future Directions

This study serves as a primary investigation into the interactions between GNPs and key proteins involved in atherosclerosis. While the in silico and in vitro approaches provide foundational insights, the absence of in vivo validation remains a limitation. In vivo models are essential to fully understand the systemic effects of GNPs on foam cell formation and lipid metabolism. Future studies should incorporate animal models to investigate long-term biological effects, including potential toxicity and biodistribution. Additionally, using other cell models relevant to foam cell formation, such as human monocyte-derived macrophages or THP-1 macrophages, would provide a more physiologically relevant representation of atherosclerosis.

Another limitation is the use of a single concentration (1 μg/mL) of GNPs. While this concentration was chosen based on previous studies and cell viability assays, a dose-response analysis would help establish the therapeutic window and ensure that GNPs do not induce cytotoxic effects at higher concentrations. Future studies should evaluate a range of concentrations to better understand dose-dependent effects.

Additionally, while this study provides valuable molecular insights through in silico and in vitro approaches, the absence of in vivo validation limits the translational potential of the findings. Future studies incorporating animal models would be essential to evaluate the systemic effects of GNPs on lipid metabolism, inflammation, and atherosclerotic plaque development. Additionally, exploring the stability and aggregation behavior of GNPs in biological environments would help determine their long-term behavior and potential interactions with physiological systems. Despite these limitations, this study provides important mechanistic insights into the role of GNPs in foam cell formation and highlights key molecular interactions that could inform future research on graphene-based materials in cardiovascular applications.

Conclusion

In conclusion, this study demonstrates that GNPs exhibit a stronger binding affinity to ApoB compared to LDLR. When combined with insights from previous in silico studies involving atherosclerosis-related proteins such as CD36, TLR4, LOX1, and SRA1, this finding suggests that GNPs may play a significant role in disrupting lipid metabolism and foam cell formation—key processes in atherosclerosis. The smaller size of the graphene models used in this study ensures a balance between computational efficiency and accuracy, enabling detailed analysis of binding behaviours and surface interactions. Complementary in vitro results further highlight GNPs' ability to inhibit macrophage-derived foam cell formation by modulating pro-atherogenic pathways. Specifically, GNPs reduce the secretion of

pro-inflammatory cytokines (IFNγ, IL-1β, and IL-6), downregulate the expression of inflammatory (IL-1β), scavenger receptor (CD36), and cholesterol esterification (ACAT-1) genes, while upregulating cholesterol efflux genes (ABCA-1). This integrated approach highlights the potential of GNPs as promising modulators of key atherosclerotic mechanisms and therapeutic candidates for atherosclerosis intervention.

Acknowledgements This work was supported by Fundamental Research Grant Scheme (FRGS) (FRGS/1/2022/SKK10/USM/02/28) funded by Ministry of Higher Education Malaysia.

Author Contributions R.M., A.N.S., M.Y.A., M.A.Z. and M.M.R. designed the research study. F.H.L. performed in silico experimental works under guidance of A.N.S. and M.Y.A., while in vitro works were assisted by M.A.Z., M.M.R. and R.M. R.M. and F.H.L. wrote the manuscript. R.M. is the principal investigator for FRGS grant that funded this research. All authors read and approved the final version of manuscript for submission.

Funding Open access funding provided by The Ministry of Higher Education Malaysia and Universiti Sains Malaysia.

Data Availability The data will be provided from the corresponding author (rafeezul@usm.my) on reasonable request.

Declarations

Conflict of interest The authors declare that they have no conflict of interest.

References

1. Weber, C., and H. Noels. Atherosclerosis: current pathogenesis and therapeutic options. *Nat. Med.* 17:1410–1422, 2011. https://doi.org/10.1038/nm.2538.
2. Libby, P., P. M. Ridker, and G. K. Hansson. Progress and challenges in translating the biology of atherosclerosis. *Nature.* 473:317–325, 2011. https://doi.org/10.1038/nature10146.
3. Wang, T., D. Palucci, K. Law, B. Yanagawa, J. Yam, and J. Butany. Atherosclerosis: pathogenesis and pathology. *Diagn. Histopathol.* 18:461–467, 2012. https://doi.org/10.1016/j.mpdhp.2012.09.004.
4. Clarke, M. C. H., and M. R. Bennett. Vascular smooth muscle cells in atherosclerosis. *Nat. Rev. Cardiol.* 16:727–744, 2019. https://doi.org/10.1038/s41569-019-0227-9.
5. Aldons, J. Lusis atherosclerosis. *Nature.* 407:233–241, 2000. https://doi.org/10.1038/35025203.Atherosclerosis.
6. Poznyak, A. V., N. G. Nikiforov, A. V. Starodubova, T. V. Popkova, and A. N. Orekhov. Macrophages and foam cells: brief overview of their role, linkage, and targeting potential in atherosclerosis. *Biomedicines.* 9:1221, 2021. https://doi.org/10.3390/biomedicines9091221.
7. Fayad, Z. A., F. K. Swirski, C. Calcagno, C. S. Robbins, W. Mulder, and J. C. Kovacic. Monocyte and macrophage dynamics in the cardiovascular system: JACC macrophage in CVD series (part 3). *J. Am. CollCardiol.* 72:2198–2212, 2018. https://doi.org/10.1016/j.jacc.2018.08.2150.
8. Javadifar, A., S. Rastgoo, M. Banach, T. Jamialahmadi, T. P. Johnston, and A. Sahebkar. Foam cells as therapeutic targets in atherosclerosis with a focus on the regulatory roles of non-coding RNAS. *Int. J. Mol. Sci.* 22:1–27, 2021. https://doi.org/10.3390/ijms22052529.
9. Zhang, X. Q., O. Even-Or, X. Xu, M. van Rosmalen, L. Lim, S. Gadde, et al. Nanoparticles containing a liver X receptor agonist inhibit inflammation and atherosclerosis in macrophages and Ldlr−/− mice. *Adv. Healthc. Mater.* 4(2):228–236, 2014.
10. Tang, J., S. Baxter, A. Menon, A. M. S. A. Alaarg, B. L. Sanchez-Gaytan, F. Fay, et al. Immune cell screening of a nanoparticle library improves atherosclerosis therapy. *Proc. Natl. Acad. Sci. U S A.* 113(44):E6731–E6740, 2016.
11. Boada, C. A., A. Zinger, S. Rohen, et al. LDL-based lipid nanoparticle derived for blood plasma accumulates preferentially in atherosclerotic plaque. *Front. Bioeng. Biotechnol.*9:794676, 2021. https://doi.org/10.3389/fbioe.2021.794676.
12. Di, L., and A. Maiseyeu. Low-density lipoprotein nanomedicines: mechanisms of targeting, biology, and theranostic potential. *Drug Deliv.* 28(1):408–421, 2021. https://doi.org/10.1080/10717544.2021.1886199.
13. Yari-Ilkhchi, A., N. Hamidi, M. Mahkam, and A. Ebrahimi-Kalan. Graphene-based materials: an innovative approach for neural regeneration and spinal cord injury repair. *RSC Adv.* 15:9829–9853, 2025.
14. Amrollahi-Sharifabadi, M., M. K. Koohi, E. Zayerzadeh, M. H. Hablolvarid, J. Hassan, and A. M. Seifalian. In vivo toxicological evaluation of graphene oxide nanoplatelets for clinical application. *Int. J. Nanomed.* 13:4757–4769, 2018.
15. Liao, C., Y. Li, and S. C. Tjong. Graphene nanomaterials: synthesis, biocompatibility, and cytotoxicity. *Int. J. Mol. Sci.* 19(11):3564, 2018.
16. Goldstein, J. L., and M. S. Brown. A century of cholesterol and coronaries: from plaques to genes to statins. *Cell.* 161(1):161–172, 2015. https://doi.org/10.1016/j.cell.2015.01.036.
17. Lat, F. H., A. N. Shuid, M. Y. Aziz, M. M. Ramli, and R. Mohamed. Exploring the interaction of graphene-based nanomaterials with atherosclerosis-related protein targets: insights from molecular docking and dynamics simulations. *J. Nanopart. Res.* 26:248, 2024.
18. Huang, B., Q. Wang, Y. Li, M. Zhang, and X. Wei. Preparation and characterisation of graphene. *Mater. Res. Innov.* 19(9):S9-344-S9-350, 2015. https://doi.org/10.1179/1432891715Z.0000000002010.
19. Derakhshi, M., S. Daemi, P. Shahini, A. Habibzadeh, et al. Two-dimensional nanomaterials beyond graphene for biomedical applications. *J. Funct. Biomater.* 13(1):27, 2022. https://doi.org/10.3390/jfb13010027.
20. Cataldi, P., A. Athanassiou, and I. S. Bayer. Graphene nanoplatelets-based advanced materials and recent progress in sustainable applications. *Appl. Sci.* 8(9):1438, 2018. https://doi.org/10.3390/app8091438.
21. Yee, K., and M. H. Ghayesh. A review on the mechanics of graphene nanoplatelets reinforced structures. *Inter. J. Eng.*

*Sci.*186:103831, 2023. https://doi.org/10.1016/j.ijengsci.2023.103831.
22. Reichel, D., M. Tripathi, and J. M. Perez. Biological effects of nanoparticles on macrophage polarization in the tumor microenvironment. *Nanotheranostics.* 3(1):66–88, 2019. https://doi.org/10.7150/ntno.30052.
23. Shu, H., Y. Peng, W. Hang, J. Nie, et al. The role of CD36 in cardiovascular disease. *Cardiovasc. Res.* 118(1):115–129, 2022. https://doi.org/10.1093/cvr/cvaa319.
24. Krivak, R., and D. Hoksza. P2Rank: machine learning-based tool for rapid and accurate prediction of ligand binding sites from protein structure. *J. Cheminform.* 10(1):39, 2018.
25. Cousins, K. R. Computer review of ChemDraw ultra 12.0. *J. Am. Chem. Soc.* 133(33):8388–8388, 2011.
26. Jakubec, D., P. Skoda, R. Krivak, M. Novotny, and D. Hoksza. PrankWeb 3: accelerated ligand-binding site predictions for experimental and modelled protein structures. *Nucleic Acids Res.* 50:593–597, 2022.
27. Trott, O., and A. J. Olson. AutoDock Vina: improving the speed and accuracy of docking with a new scoring function, efficient optimization, and multithreading. *J. Comput. Chem.* 31:455–461, 2010.
28. Durrant, J. D., and J. A. McCammon. BINANA: a novel algorithm for ligand-binding characterization. *J. Mol. Graph. Model.* 29(6):888–893, 2011.
29. Zhang, J., M. Zamani, C. Thiele, J. Taher, M. A. Alipour, Z. Yao, and K. Adeli. AUP1 (ancient ubiquitous protein 1) is a key determinant of hepatic very-low-density lipoprotein assembly and secretion. *Arterioscler. Thromb. Vasc. Biol.* 37(6):1093–1102, 2017.
30. Fass, D., S. C. Blacklow, P. S. Kim, and J. M. Berger. Molecular basis of familial hypercholesterolaemia from structure of LDL receptor module. *Nature.* 388(6643):691–693, 1997.
31. Chen, J., Y. Su, S. Pi, B. Hu, and L. Mao. The dual role of low-density lipoprotein receptor-related protein 1 in atherosclerosis. *Front. Cardiovasc. Med.*8:682389, 2021.
32. Witztum, J. L. Theoretical mechanisms by which macrophage foam cells could be generated. *J. Clin. Invest.* 115(8):2072–2075, 2005.
33. Cauet, E., M. Rooman, R. Wintjens, J. Lievin, and C. Biot. Histidine-aromatic interactions in proteins and protein-ligand complexes: Quantum chemical study of X-ray and model structures. *J. Chem. Theory Comput.* 1:472–483, 2005.
34. Lu, Y., Y. Wang, and W. Zhu. Nonbonding interactions of organic halogens in biological systems: implications for drug discovery and biomolecular design. *Phys. Chem. Chem. Phys.* 12:4543–4551, 2010.
35. Chen, K., and L. Kurgan. Investigation of atomic level patterns in protein-small ligand interactions. *PLoS One.* 4:4473, 2009.
36. Casalini, T., V. Limongelli, M. Schmutz, C. Som, O. Jordan, P. Wick, G. Borchard, and G. Perale. Molecular modeling for nanomaterial–biology interactions: Opportunities, challenges, and perspectives. *Front. Bioeng. Biotechnol.* 7:268, 2019.
37. Tuffery, P., and P. Derreumaux. Flexibility and binding affinity in protein–ligand, protein–protein and multi-component protein interactions: limitations of current computational approaches. *J. R. Soc. Interface.* 9(66):20–33, 2012.
38. Sudhan, M., V. Janakiraman, S. F. Ahmad, S. M. Attia, T. B. Emran, R. B. Patil, and S. S. J. Ahmed. Structural characteristics of PON1 with Leu55Met and Gln192Arg variants influencing oxidative-stress-related diseases: an integrated molecular modeling and dynamics study. *Medicina.* 59(12):2060, 2023.
39. Boehr, D. D., R. Nussinov, and P. E. Wright. The role of dynamic conformational ensembles in biomolecular recognition. *Nat. Chem. Biol.* 5(11):789–796, 2009.
40. Tuntufye, E., L. Paul, J. Raymond, M. Chacha, A. S. Paluch, and D. M. Shadrack. In silico analysis of vitamin D interactions with aging proteins: docking, molecular dynamics, and solvation free energy studies. *Chem. Eng.* 8(5):104, 2024.
41. Poater, J., M. Swart, F. M. Bickelhaupt, and G. C. Fonseca. B-DNA structure and stability: the role of hydrogen bonding, π–π stacking interactions, twist-angle, and solvation. *Org. Biomol. Chem.* 12(27):4691–4700, 2014.
42. Kudin, K. N., B. Ozbas, H. C. Schniepp, R. K. Prud'homme, I. A. Aksay, and R. Car. Raman spectra of graphite oxide and functionalized graphene sheets. *Nano Lett.* 8(1):36–41, 2008.
43. Meng, X. Y., H. X. Zhang, M. Mezei, and M. Cui. Molecular docking: a powerful approach for structure-based drug discovery. *Curr. Comput. Aided Drug Des.* 7(2):146–157, 2011.
44. Bagri, A., C. Mattevi, M. Acik, Y. J. Chabal, M. Chhowalla, and V. B. Shenoy. Structural evolution during the reduction of chemically derived graphene oxide. *Nat. Chem.* 2(7):581–587, 2010.
45. Firdaus, R. M., B. Vigolo, and A. R. Mohamed. Enhanced functionalization of graphene nanoplatelets through sulfonitric treatment: investigating optimal conditions via FTIR analysis. *Malays. J. Chem.* 26(3):127–133, 2024.
46. Xu, S., Y. Huang, Y. Xie, et al. Evaluation of foam cell formation in cultured macrophages: an improved method with Oil Red O staining and DiI-oxLDL uptake. *Cytotechnology*. 62:473–481, 2010. https://doi.org/10.1007/s10616-010-9290-0.
47. Kitko, K. E., T. Hong, R. M. Lazarenko, D. Ying, et al. Membrane cholesterol mediates the cellular effects of monolayer graphene substrates. *Nat. Commun.* 9(1):796, 2018. https://doi.org/10.1038/s41467-018-03185-0.
48. Kang, I., J. M. Yoo, D. Kim, J. Kim, et al. Graphene quantum dots alleviate impaired functions in Niemann-Pick disease type C in vivo. *Nano Lett.* 21(5):2339–2346, 2021.
49. Luo, Y., J. Peng, C. Huang, and Y. Cao. Graphene oxide size-dependently altered lipid profiles in THP-1 macrophages. *Ecotoxicol. Environ. Saf.*199:110714, 2020. https://doi.org/10.1016/j.ecoenv.2020.110714.
50. Luo, Y., X. Wang, and Y. Cao. Transcriptomic analysis suggested the involvement of impaired lipid droplet biogenesis in graphene oxide-induced cytotoxicity in human umbilical vein endothelial cells. *Chem. Biol. Interact.*333:109325, 2021. https://doi.org/10.1016/j.cbi.2020.109325.
51. Luo, Y., J. Li, C. Huang, X. Wang, D. Long, and Y. Cao. Graphene oxide links alterations of anti-viral signaling pathways with lipid metabolism *via* suppressing TLR3 in vascular smooth muscle cells. *Mol. Omics.* 18(8):779–790, 2022. https://doi.org/10.1039/d2mo00086e.
52. Liu, X., C. Yang, P. Chen, L. Zhang, and Y. Cao. The uses of transcriptomics and lipidomics indicated that direct contact with graphene oxide altered lipid homeostasis through ER stress in 3D human brain organoids. *Sci. Total Environ.*849:157815, 2022. https://doi.org/10.1016/j.scitotenv.2022.157815.
53. Harvey, E. J., and D. P. Ramji. Interferon-gamma and atherosclerosis: pro- or anti-atherogenic? *Cardiovasc. Res.* 67:11–20, 2005. https://doi.org/10.1016/j.cardiores.2005.04.019.
54. Moss, J. W. E., and D. P. Ramji. Interferon-γ: promising therapeutic target in atherosclerosis. *World J. Exp. Med.* 5(3):154–159, 2015. https://doi.org/10.5493/wjem.v5.i3.154.
55. Liu, W., Y. Yin, Z. Zhou, M. He, and Y. Dai. OxLDL-induced IL-1 beta secretion promoting foam cells formation was mainly via CD36 mediated ROS production leading to NLRP3 inflammasome activation. *Inflamm. Res.* 63(1):33–43, 2014. https://doi.org/10.1007/s00011-013-0667-3.
56. Allison, B. R., M. S. Nicolle, and D. L. Joshua. Interleukin-6 in atherosclerosis: atherogenic or atheroprotective? *Clin. Lipidol.* 12(1):14–23, 2017. https://doi.org/10.1080/17584299.2017.1319787.

57. Zheng, Y., N. Pescatore, Y. Gogotsi, B. Dyatkin, et al. Rapid adsorption of proinflammatory cytokines by graphene nanoplatelets and their composites for extracorporeal detoxification. *J. Nanomater.* 2018:6274072, 2018. https://doi.org/10.1155/2018/6274072.
58. Yin, K., D. F. Liao, and C. K. Tang. ATP-binding membrane cassette transporter A1 (ABCA1): a possible link between inflammation and reverse cholesterol transport. *Mol. Med.* 16(9–10):438–449, 2010. https://doi.org/10.2119/molmed.2010.00004.
59. Schinwald, A., F. A. Murphy, A. Jones, W. MacNee, and K. Donaldson. Graphene-based nanoplatelets: a new risk to the respiratory system as a consequence of their unusual aerodynamic properties. *ACS Nano.* 6(1):736–746, 2012. https://doi.org/10.1021/nn204229f.
60. Adamson, S. X. F., R. Wang, W. Wu, B. Cooper, and J. Shannahan. Metabolomic insights of macrophage responses to graphene nanoplatelets: role of scavenger receptor CD36. *PLoS ONE.* 13(11):e0207042, 2018. https://doi.org/10.1371/journal.pone.0207042.
61. He, J., W. Zhang, X. Zhou, F. Xu, et al. Reactive oxygen species (ROS)-responsive size-reducible nanoassemblies for deeper atherosclerotic plaque penetration and enhanced macrophage-targeted drug delivery. *Bioact. Mater.* 19:115–126, 2022.
62. Dhanasekara, C. S., J. Zhang, S. Nie, G. Li, Z. Fan, and S. Wang. Nanoparticles target intimal macrophages in atherosclerotic lesions. *Nanomedicine.*29(32):102346, 2020.
63. Petersen, L. K., A. W. York, D. R. Lewis, S. Ahuja, K. E. Uhrich, R. K. Prud'homme, and P. V. Moghe. Amphiphilic nanoparticles repress macrophage atherogenesis: novel core/shell designs for scavenger receptor targeting and down-regulation. *Mol. Pharm.* 11(8):2815–2824, 2014.
64. Zhang, J., S. Nie, Y. Zu, M. Abbasi, J. Cao, C. Li, D. Wu, S. Labib, G. Brackee, C. L. Shen, and S. Wang. Anti-atherogenic effects of CD36-targeted epigallocatechin gallate-loaded nanoparticles. *J. Control Release.* 303:263–273, 2019.
65. Sun, W., Y. Xu, Y. Yao, J. Yue, et al. Self-oxygenation mesoporous MnO_2 nanoparticles with ultra-high drug loading capacity for targeted arteriosclerosis therapy. *J. Nanobiotech.*20:882022, 2022.
66. Dai, T., W. He, S. Tu, J. Han, et al. Black TiO_2 nanoprobe-mediated mild phototherapy reduces intracellular lipid levels in atherosclerotic foam cells via cholesterol regulation pathways instead of apoptosis. *Bioact. Mater.* 17:18–28, 2022.
67. Gurunathan, S., M. H. Kang, M. Jeyaraj, J. H. Kim, et al. Differential cytotoxicity of different sizes of graphene oxide nanoparticles in Leydig (TM3) and Sertoli (TM4) cells. *Nanomaterials.* 9(2):139, 2019.
68. Mu, Q., G. Su, L. Li, B. O. Gilbertson, L. H. Yu, Q. Zhang, Y. P. Sun, and B. Yan. Size-dependent cell uptake of protein-coated graphene oxide nanosheets. *ACS Appl. Mater. Interfaces.* 4(4):2116–2123, 2012.
69. Wang, D. D., M. Zhu, and H. Yan. Computationally predicting binding affinity in protein–ligand complexes: Free energy-based simulations and machine learning-based scoring functions. *Brief Bioinform.* 22(3):bba107, 2020.
70. Gu, S., C. Shen, J. Yu, H. Zhao, H. Liu, L. Liu, R. Sheng, L. Xu, Z. Wang, and T. Hou. Can molecular dynamics simulations improve predictions of protein-ligand binding affinity with machine learning? *Brief Bioinform.* 24(2):bbad008, 2023.
71. Ganji, N., and G. D. Bothun. Albumin protein coronas render nanoparticles surface active: consonant interactions at air–water and at lipid monolayer interfaces. *Soft Matter.* 17:3705–3715, 2021.
72. Guglielmelli, A., P. D'Aquila, G. Palermo, M. Dell'Aglio, G. Passarino, G. Strangi, and D. Bellizzi. Role of the human serum albumin protein corona in the antimicrobial and photothermal activity of metallic nanoparticles against *Escherichia coli* bacteria. *ACS Omega.* 8(34):31333–31343, 2023.
73. Liu, X., C. Yan, and K. L. Chen. Adsorption of human serum albumin on graphene oxide: implications for protein corona formation and conformation. *Environ. Sci. Technol.* 53(15):8631–8639, 2019.
74. Quagliarini, E., D. Pozzi, F. Cardarelli, and G. Caracciolo. The influence of protein corona on graphene oxide: implications for biomedical theranostics. *J. Nanobiotechnol.* 21:267, 2023.